"西光所建所六十周年暨《光子学报》创刊五十周年"专辑

基于飞秒激光的超快太赫兹特征波谱技术及其应用(特邀)

范文慧,闫慧,江晓强,陈龙超,郑转平,刘佳,李慧,丁玲,宋超

(中国科学院西安光学精密机械研究所 瞬态光学与光子技术国家重点实验室, 西安 710119)

摘　要：太赫兹特征波谱技术作为一种太赫兹波段的相干测量技术,具有高灵敏、快速、无损检测等显著特点,可以有效获得来源于物质分子的低频集体振动、转动模式以及与周围分子的弱相互作用(氢键、范德华力等)而产生的特征"指纹谱"信息,已在生化分子检测、材料分析与辨识等方面展现出非常广阔的应用前景。太赫兹光电导天线作为一类应用广泛的太赫兹波源,能够产生宽频带的太赫兹辐射,由其构成的超快太赫兹特征波谱系统在生化分子和材料分析等方面已显现重要应用。本文首先介绍了基于超短脉冲激光的太赫兹光电导天线的工作原理及其发展现状,包括理论模型、衬底材料以及不同结构形式。随后,介绍了由太赫兹光电导天线作为宽频带太赫兹波源而构建的超快太赫兹特征波谱系统及其工作机理,详细阐述了基于飞秒激光的超快太赫兹特征波谱技术及其应用取得的一些最新研究进展,并分析讨论了该技术在实际应用过程中面临的挑战和应对策略。

关键词：太赫兹波；光电导天线；飞秒激光；特征波谱；物质辨识；机器学习

中图分类号：TN36；O433　　　　**文献标识码**：A　　　　**doi**：10.3788/gzxb20225107.0751403

0　Introduction

The practical applications of Terahertz (THz) waves can tremendously reconstruct our living conditions in the next decades, including terabit wireless communications [1], hidden-object inspection [2], fingerprint identification of chemicals [3], biomedical imaging [4], space exploration [5], and so on. As the fundamental devices, the THz emitters and detectors have been widely investigated along with the development of THz technology. However, the radiation power, optical-to-THz conversion efficiency, and operation bandwidth of THz emitters as well as the sensitivity, response frequency range, and intrinsic noise of THz detectors can hardly meet the strict requirements of current applications [6]. In order to bring these advanced technologies into our daily scenarios, the bright THz emitters and sensitive THz detectors are urgently required for enhancing the THz systems. Therefore, the investigation of THz emitters and detectors still remains for further development.

THz Photoconductive Antenna (THz-PCA), as one of the promising THz emitters and detectors, has the advantages to overcome the defects confronted by other devices (e.g., low operation frequency, strict working condition and bulk size) and make THz-PCA very attractive by meeting the requirements of broadband frequency, room temperature operation and compact size [7-9]. Generally, THz-PCA composed of metallic antenna deposited on a photoconductor with sub-picosecond carrier lifetime. When the femtosecond laser pulses are incident on the photoconductor, the photocarriers will be generated in the active area and driven by external bias voltage to produce photocurrent towards the electrodes and subsequently radiate THz waves [9]. With the

http：∥www.photon.ac.cn

development of ultrashort laser technology, Auston et al. generated the photocurrent within the picosecond timescale by employing the "Auston switch", which was considered as the prototype of THz-PCA [10]. Since then, the THz-PCA has been widely investigated as both emitters and detectors remarkably facilitating the development of THz technology. For example, GRISCHKOWSKY D et al. developed the THz Time-Domain Spectroscopy (THz-TDS) by utilizing the THz-PCAs, which has been widely utilized in THz characteristic spectroscopy and material identification [11].

Nowadays, with the dramatic development of emitter and detector components, THz-TDS have become the most commonly used technique in current commercial THz spectroscopy [12] with advantages of coherent measurement, spectral fingerprint, high time and spatial resolution. After years of extensive works, both in experiment and calculation [13-14], it has been verified that THz spectra represent a characteristic "fingerprint" of molecular substance [15-16]. Therefore, various substances can be effectively recognized and characterized according to their distinctive THz features. Moreover, the characteristic absorption peaks of substances in THz region are associated with intermolecular collective modes of the hydrogen-bonding network and low-frequency intramolecular modes of molecules [17-18], so they are very sensitive to the molecular structure and surrounding environment. Even for the molecules with the same molecular formula, slight differences in their molecular structures can also generate significant different spectral features in their THz spectra. Therefore, THz-TDS can be used as a powerful tool to investigate molecular conformation [19], positional isomerism of functional groups [20], cis-trans isomerism [21], optical isomerism [22], and the influence of environment on intermolecular force, such as temperature, aqueous environment, ionic interaction [23]. However, another issue worth noting is that the investigated targets are usually in the form of multi-component mixtures in actual scenario. When the spectral features became more complicated, the much broader THz features would be severely overlapped and accompanied by baseline drift in THz spectra. Identification and quantitative analysis of complex multi-component mixtures will become a great challenge for THz spectral analysis. To overcome such problem, we propose a practical strategy by combining machine learning methods with THz-TDS for implementation of practical applications [24]. In this paper, the recent progress we have achieved in THz characteristic spectral technology and its applications are also summarized and discussed.

1 Classification of THz emitters and detectors

As the indispensable elements in THz technology, the efficiency of THz emitters and detectors can directly determine the operation performances of THz systems. Numerous approaches have been proposed to improve the efficiency of THz emitters and detectors, and great achievements have also been accomplished in the past decades. In order to further promote the research interests of THz emitters and detectors, the major methods and classification of THz emitters and detectors are summarized in this section.

1.1 Classification of THz emitters

THz waves (0.1 THz~10 THz, 1 THz $= 10^{12}$ Hz) locate in the transitional region of the electromagnetic spectrum, between the classical electronics (radio, microwave and millimeter wave) and the photonics (infrared, visible, ultraviolet and X-ray) in which the quantum nature is dominant. Therefore, the generation of THz waves can be roughly divided into three major categories [25-26]: 1) electronics, 2) photonics, and 3) ultrafast optoelectronics, as depicted in Fig. 1.

The THz sources made from electronic devices, including backward-wave oscillator [26], solid-state integrated circuit [27], microwave multiplier [28], and nonlinear transmission line [29], generally increase the working frequency of classical microwave devices toward low-frequency of THz band. The photonic methods normally include optical rectification [30], laser-induced air plasma [31], nonlinear frequency conversion [32], optically pumped gas laser [33]. With the remarkable progress in ultrafast lasers and low-dimensional semiconductor materials, ultrafast optoelectronic methods for generating THz radiation have been rapidly developed, which include THz-PCA [8], THz photomixer [25], free-electron laser [34], Quantum Cascade Laser (QCL) [35], semiconductor surface [36], and so on. Moreover, some novel methods for THz generation by using ultrafast lasers have also been proposed recently [37-39], such as spintronic THz source and dielectric metasurface, which have shown a great potential for promoting the development of THz technologies.
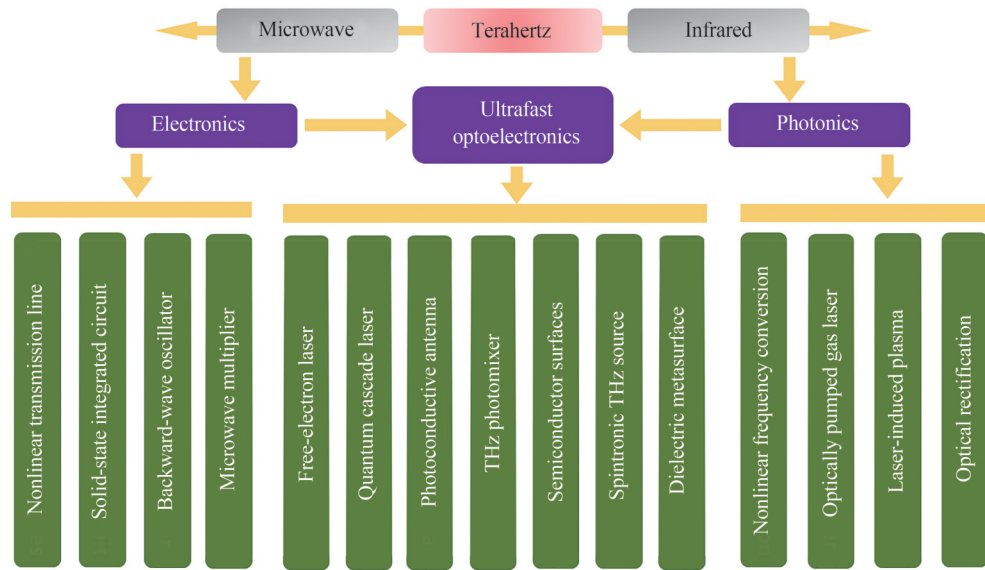
Fig. 1   The classification of typical THz emitters

Although numerous approaches have been proposed for THz wave generation, the big challenges still remain and hinder the further development of THz technologies. Electronic devices for THz generation have intrinsic defects attributed to the resistor-capacitor roll-off and transit-time roll-off, resulting in a severe power loss at high THz frequencies [40]. It should be noted that some chip-scale electronic devices, including Gunn diode, Schottky multiplier, and impact ionization avalanche transit-time diode, have the ability to supply high power, high purity spectrum, and attractive tunability in the low THz frequencies ($<$ 0.5 THz). However, the electronic devices can hardly be operated at the higher THz frequencies beyond 1 THz, which is extremely important frequency range for the THz applications. On the other hand, the strict operation environments are inevitably required for certain THz sources. For instance, the QCLs can emit the THz waves with watt-level radiation power and broad tunable ranges only at cryogenic environment [35]. Besides, the physical mechanism and fabrication techniques for spintronic THz source and dielectric metasurface are not as mature as the conventional devices; thereby they can hardly meet the requirements of practical applications.

In fact, the THz-PCAs have the distinct advantages for THz generation, making them very attractive for the requirements of broadband frequency, room temperature operation and compact size. Both the physical mechanism and research progress of THz-PCA emitters are detailly analyzed in the Section 2 and Section 4, respectively.

1.2   Classification of THz detectors

The THz detection can be divided into two major categories according to their coherence [41], namely, coherent detection and incoherent detection. The coherent detection refers to the detector that is sensitive to the phase and amplitude of the received THz signal. On the other hand, incoherent detection is the detector that is only sensitive to the amplitude of the received THz signal.

The coherent detection of THz waves is tightly related to the THz generation because they usually share the same pump laser and the similar physical mechanism. The photoconductive receiver and electro-optic detection are normally employed for the detection of coherent broadband THz waves. Meanwhile, the heterodyne detector and photomixer receiver are normally used for the detection of Continuous-Wave (CW) THz waves. On the other hand, the pyroelectric detector, bolometer, and Golay cell are the common devices for incoherent detection of THz signal. Similarly, both the physical mechanism and research progress of THz-PCA detectors are detailly analyzed in the Section 3 and Section 4, respectively.
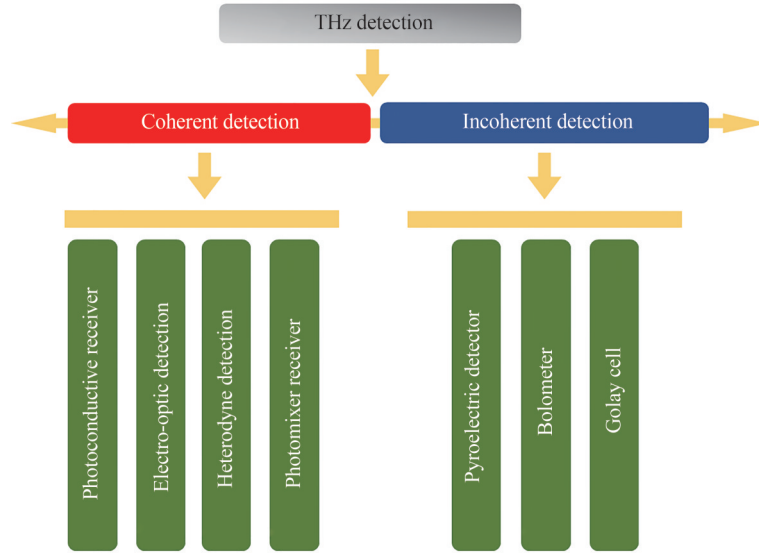
Fig. 2　The classification of typical THz detectors

2　Physical mechanism of THz-PCA emitter

The schematic of the pulsed THz radiation from a THz-PCA is depicted in Fig. 3. The THz-PCA is normally consisted of a biased metal antenna deposited on a photoconductive substrate [8]. The femtosecond pump laser is directly incident on the antenna gap and transmits into the photoconductor. Because the energy gap of the photoconductor is less than the photon energy of the pump laser, the photocarriers will be generated inside the photoconductor as the pump laser is absorbed. Moreover, under the influence of bias field, the generated photocarriers are accelerated to produce the transient photocurrent, which drives the metal antenna to emit the pulsed THz waves finally.
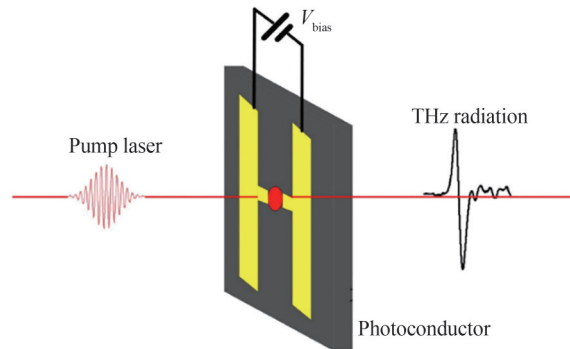
Fig. 3　Schematic of THz radiation from a THz-PCA excited by femtosecond pump laser

To investigate the underlying physical mechanism of the transient response in THz-PCA, the influence of several parameters, such as the power intensity of femtosecond pump laser, the laser pulse duration and the carrier lifetime of the substrate material, are analyzed based on the current surge model [9,42].

2.1　The characteristics of generated photocarriers under different conditions

Considering the incident femtosecond pump laser in a Gaussian profile, the corresponding incident laser power can be described as [43]

$$P(t) = P_0 \exp\left(-\frac{t^2}{\delta_t^2}\right) \tag{1}$$

where P_0 is the peak power of pump laser and δ_t is the pulse duration of pump laser.

After the illumination of femtosecond laser, the generation rate of photocarriers in the photoconductor $G(t)$ can be obtained as [43]

$$G(t) = G_0 \exp\left(-\frac{t^2}{\delta_t^2}\right) = \frac{\eta}{hf} P_0 \tag{2}$$

where G_0 is the peak generation rate of photocarriers corresponding to P_0, η is the quantum efficiency of photoconductor, h is the Planck constant, and f is the photon frequency of pump laser.

The photocarriers can be constantly generated in the photoconductor under the illumination of femtosecond laser. However, the recombination of photocarriers also exists due to the limited photocarriers life-time τ_c. Therefore, the first-order time derivative photocarriers concentration dn/dt is depended on the dynamic process between generation and recombination [43]

$$\frac{dn(t)}{dt} = -\frac{n(t)}{\tau_c} + G(t) = -\frac{n(t)}{\tau_c} + G_0 \exp\left(-\frac{t^2}{\delta_t^2}\right) \tag{3}$$

where $n(t)$ is the time-dependent photocarriers concentration.

In order to solve the Eq. (3), the boundary conditions of $n(t = 0) = 0$ and $n(t \to -\infty) = 0$ are considered. Accordingly, by solving Eqs. (1)~(3), the ultrafast dynamics between the interactions of pump laser and THz-PCA can be theoretically analyzed. Here, the generated photocarrier density under different conditions, including the peak power and the pulse duration of pump laser as well as the life-time of photocarriers, are detailly investigated.

2.1.1 Dependence of laser peak power

According to Eq. (2), the generation rate of photocarriers is directly depended on the peak power of pump laser. Therefore, the peak carrier generation rate G_0 is set as the variable to describe the varied peak power of pump laser in this section. Meanwhile, the life-time of photocarriers τ_c and the pulse duration of pump laser δ_t is set as $\tau_c = 1$ ps, and $\delta_t = 25$ fs, respectively.

The simulated time-domain characteristics of the carrier density are depicted in Fig. 4(a). It is clear that there are two main stages of the photocarriers: generation and decay, which is depended on the pulse duration of pump laser and the life-time of photocarriers, respectively. In Fig. 4(b), the partial profile indicates that the rise time of carrier density increases to the maximum is around 25 fs, which is basically equal to the pulse duration. After then, the carrier density rapidly decreases due to the trap in the bandgap of photoconductor and the recombination of photocarriers.

(a) The simulated carrier density   (b) The partial enlarged profile
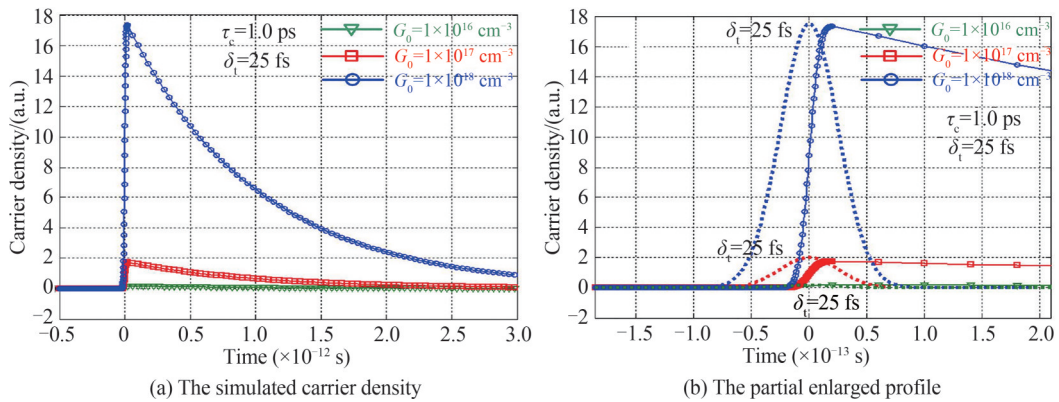
Fig. 4   The simulated time-domain characteristics of the carrier density corresponding to different peak powers of pump laser ($G_0 = 1 \times 10^{16}$ cm^{-3}, 1×10^{17} cm^{-3} and 1×10^{18} cm^{-3})

2.1.2 Dependence of laser pulse duration

Here, the pulse duration of pump laser δ_t is set as the variable. The life-time of photocarriers τ_c and the peak generation rate of photocarriers G_0 is set as $\tau_c = 1$ ps, and $G_0 = 1 \times 10^{18}$ cm^{-3}, respectively.

From Fig. 5(a), although the pulse durations of pump laser are varied, the decay time of photocarriers is barely changed due to identical carrier life-time. The time required for the carrier density to decrease to half of the maximum value is around 1 ps in three cases, as depicted in Fig. 5(b). However, the pulse duration of pump laser can affect the carrier density, and the longer pulse duration can increase the generation of photocarriers because it implies more photons from the pump laser interact with photoconductor under the same peak power.

(a) The simulated carrier density

(b) The partial enlarged profile
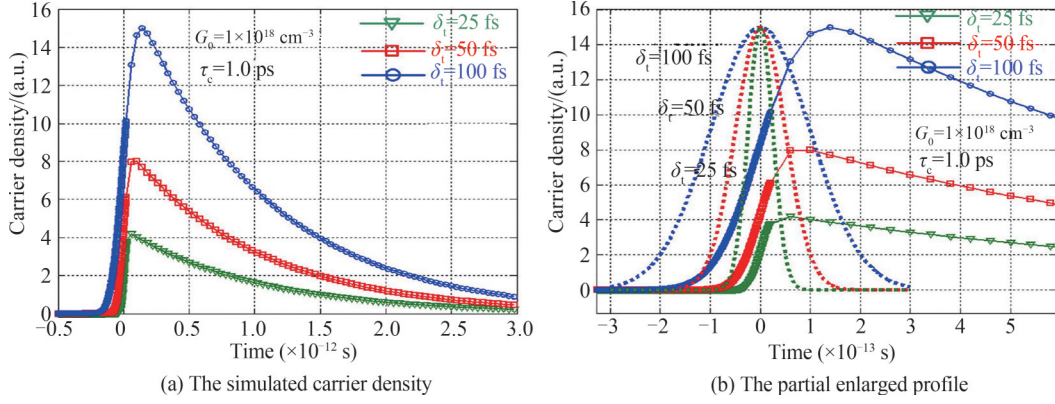
Fig. 5　The simulated time-domain characteristics of the carrier density under different pulse durations of pump laser ($\delta_t = 25$ fs, 50 fs, and 100 fs)

2.1.3　*Dependence of photocarrier life-time*

In this section, the life-time of photocarriers τ_c is set as the variable. The peak generation rate of photocarriers G_0 and the pulse duration of pump laser δ_t is set as $G_0 = 1 \times 10^{18}$ cm^{-3} and $\delta_t = 25$ fs, respectively.

In order to investigate the relationship between the decay of photocarriers and their life-time, we have also calculated the time-domain profile of generated photocarrier density under the different carrier life-times, as depicted in Fig. 6. It is clear that the decay time of photocarriers with longer carrier life-time is slower than that of the photocarriers with shorter carrier life-time, as shown in Fig. 6(a). In Fig. 6(b), the rising edges of carrier density of all three cases are almost identical due to the same pulse duration of pump laser. However, the maximum carrier density is proportional to the carrier life-time. To be specific, the photocarrier with longer carrier life-time indicates the slower decay process, which can provide more accumulation time of the photocarriers and thus the increased carrier density.

(a) The simulated carrier density

(b) The partial enlarged profile
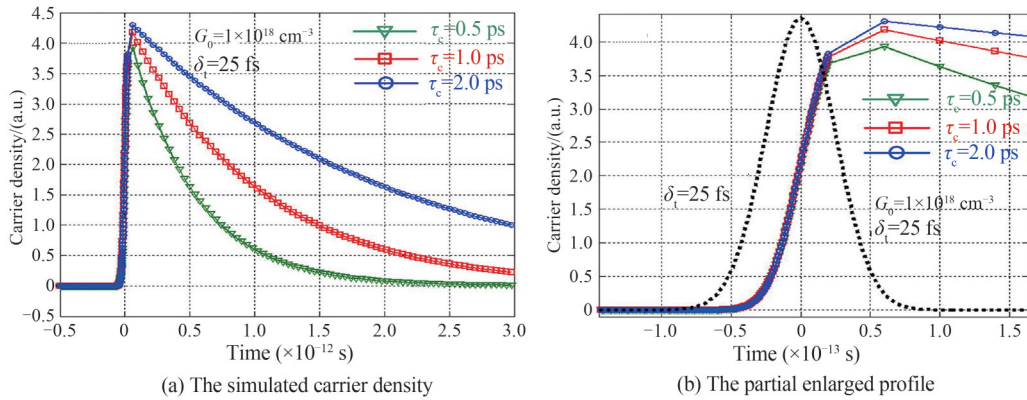
Fig. 6　The simulated time-domain characteristics of the carrier density under different carrier life-times ($\tau_c = 0.5$ ps, 1 ps, and 2 ps)

2.2　The characteristics of transient photocurrent under different conditions

The generated photocarriers accelerated to produce the transient photocurrent $J(t)$ under the bias field can be defined as

$$J(t) = qn(t)v(t) \tag{4}$$

where q is the elementary charge, and $v(t)$ is the drift velocity of the photocarrier.

According to the Drude-Lorentz model[44], the photocarriers are accelerated under the bias field with the accelerated velocity a

$$a = \frac{qE}{m^*} \tag{5}$$

where m^* is the effective mass of photocarriers, and E is the electric field in the photoconductor

$$E = E_{\mathrm{b}} - \frac{P}{3\varepsilon_0} \tag{6}$$

where E_{b} is the bias field, ε_0 is the permittivity in vacuum, and P is the polarization intensity

$$\frac{\mathrm{d}P(t)}{\mathrm{d}t} = J(t) - \frac{P(t)}{\tau_{\mathrm{r}}} \tag{7}$$

where τ_{r} is the recombination time of photocarriers.

Moreover, taking the relaxation time of photocarriers τ_{s} into consideration, the differential rate equation of the photocarriers velocity $v(t)$ can be defined as

$$\frac{\mathrm{d}v(t)}{\mathrm{d}t} = -\frac{v(t)}{\tau_{\mathrm{s}}} + \frac{qE}{m^*} \tag{8}$$

The time-domain profile of the transient photocurrent and its characteristics under different conditions can be obtained by solving Eqs. (4)~(8). The parameters used in the simulation are：$q = 1.602 \times 10^{-19}$ C, $m^* = 0.056\ m_0$, $\tau_r = 10$ ps, $\tau_s = 30$ fs, and $E_{\mathrm{b}} = 2 \times 10^6$ V/m.

2.2.1 *Dependence of photocarrier life-time*

In this case, the life-time of photocarriers τ_c is set as the variable. The peak generation rate of photocarriers G_0 and the pulse duration of pump laser δ_t is set as $G_0 = 1 \times 10^{18}$ cm^{-3} and $\delta_t = 25$ fs, respectively.

In Fig.7（a）, the transient photocurrent rises rapidly and then decreases slowly. Meanwhile, the transient photocurrent with shorter carrier life-time corresponds to the faster decreases due to its higher carrier capture rate. Similar to the generated photocarriers, the time of transient photocurrent increase to the maximum is around 25 fs that is basically equal to the pulse duration, as shown in the Fig. 7(b). Therefore, the rising edge of the transient photocurrent pulse is related to the pulse duration of pump laser, but barely relevant to the carrier life-time. It is also worth to notice that induced photocurrent under the higher carrier life-time can only slightly increase the peak photocurrent density, but the bandwidth of the photocurrent in time-domain is clearly broadened. Although the increased photocurrent density is important for THz radiation, the bandwidth of the photocurrent in time-domain also has significant influence for THz generation. Therefore, further investigation is necessary to choose the suitable photoconductor, which is concluded in Section 2.3.1.

(a) The simulated current density (b) The partial enlarged profile
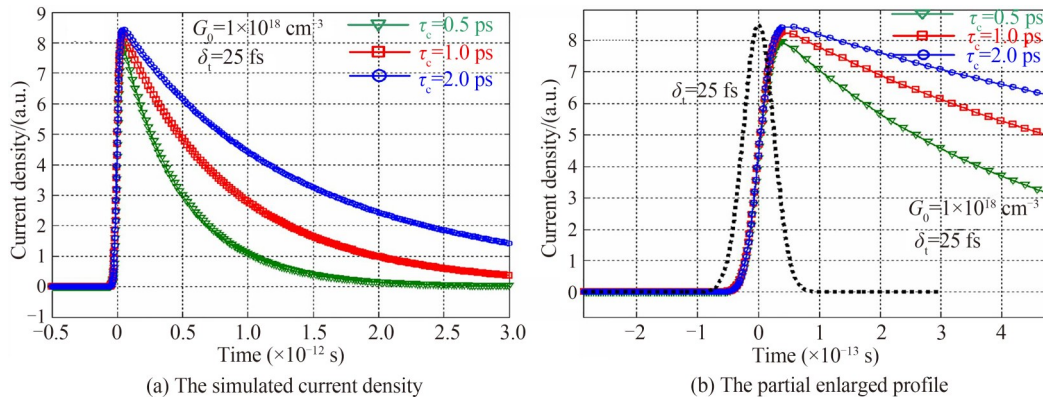
Fig. 7 The calculated time-domain characteristics of photocurrent density under different carrier life-times（$\tau_c = 0.5$ ps, 1 ps, and 2 ps）

2.2.2 *Dependence of laser pulse duration*

Here, the pulse duration of pump laser δ_t is set as the variable. The life-time of photocarriers τ_c and the peak generation rate of photocarriers G_0 is set as $\tau_c = 1$ ps, and $G_0 = 1 \times 10^{18}$ cm^{-3}, respectively.

Fig. 8（a）shows the pulse duration of pump laser has clear influence on both amplitude and bandwidth of the time-domain current density. Under the same peak power corresponding to the fixed peak generation rate of photocarriers G_0, the pump laser with longer pulse duration can carry more photons, which can excite more photocarriers and strengthen the photocurrent after the illumination. In addition, although the rise time of the photocurrent is proportion to the pulse duration of pump laser, the decay time of the photocurrent is barely affected by the pulse duration due to the fixed life-time of photocarriers, as depicted in Fig. 8(b).

(a) The simulated current density　　　　　　　(b) The partial enlarged profile
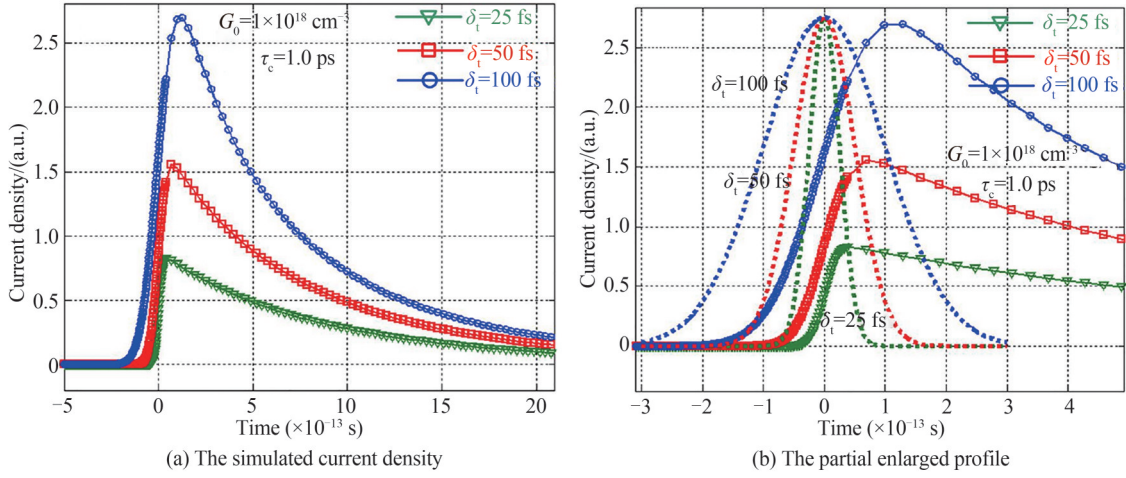
Fig. 8　The calculated time-domain characteristics of current density under different pulse durations of pump laser ($\delta_t = 25$ fs, 50 fs, and 100 fs)

2.2.3　*Dependence of laser peak power*

In this section, the peak carrier generation rate G_0 is set as the variable corresponding to the varied peak power of pump laser. Meanwhile, the life-time of photocarriers τ_c and the pulse duration of pump laser δ_t is set as $\tau_c = 1$ ps, and $\delta_t = 25$ fs, respectively.

According to Fig. 9, the peak power of pump laser can largely affect the transient photocurrent in time-domain. With the increased peak power corresponding to the increased peak carrier generation rate G_0, not only the amplitude of transient photocurrent increases, but also its time-domain bandwidth becomes narrower, which can eventually improve the THz radiation power. This can be understood as follows: the low peak power of pump laser just generates very few photocarriers, and the screening field formed by space charge separation can also be negligible compared with the bias field. Under the low peak power of pump laser, the slowly increased screening field makes the carrier velocity become saturated and the photocurrent decreases slowly. On the contrary, the high peak power of pump laser will enhance the screening field strongly, causing the photocurrent to drop rapidly and even appear negative overshoot, which is benefit for improving the THz radiation power.
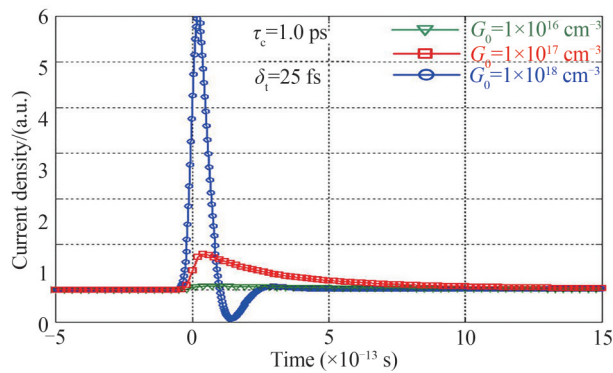
Fig. 9　The simulated time-domain profile of transient photocurrent under different peak powers of pump laser ($G_0 = 1 \times 10^{16}$ cm^{-3}, 1×10^{17} cm^{-3} and 1×10^{18} cm^{-3})

2.3　The characteristics of generated THz waves

In general, the conventional THz-PCAs can be classified to two main groups according to their antenna gap: 1) small aperture THz-PCA, which refers to the one with antenna gap smaller than the wavelength of generated THz waves; and 2) large aperture THz-PCA, which refers to the one with antenna gap larger than the wavelength of generated THz waves. In this section, the theoretical model of small aperture THz-PCA has been employed as the example to explain the physical mechanism of THz-PCA emitter.

For small aperture THz-PCA, the THz radiation mode can be considered as the normal electric dipole radiation and its far-field ($r \gg \lambda$) radiation intensity E_r can be obtained from the generated photocurrent [45]

$$E_r(r,t) \propto \frac{\partial J(r,t)}{\partial t} \qquad (9)$$

It can be seen from Eq. (9), the far-field radiation intensity of the small aperture THz-PCA is proportional to the first-order time derivative of the photocurrent. The time-domain and its Fourier-transformed THz spectra under different carrier life-times and different pulse durations as well as different peak powers of pump laser have also been investigated as follows.

2.3.1   *Dependence of photocarrier life-time*

In this case, the life-time of photocarriers τ_c is set as the variable. The peak generation rate of photocarriers G_0 and the pulse duration of pump laser δ_t is set as $G_0 = 1 \times 10^{18}$ cm^{-3} and $\delta_t = 25$ fs, respectively.

Fig. 10 depicts the relationship between the peak amplitude of THz radiation and the carrier life-time of photoconductor. It can be seen from Fig. 10(a) that the positive peak amplitudes of THz radiation under different carrier life-times are almost identical to each other, while the negative peak amplitude is slightly different. Because the proportional relationship between the generated THz waves and the first-order time derivative of the photocurrent, the positive peak amplitudes of THz radiation originate from the rising edge of the photocurrent, while the negative peak amplitude come from the falling edge of the photocurrent. As previously discussed in Fig. 7, the THz-PCA with short carrier lifetime has the rapidly decreased photocurrent; thereby it has the large time derivative corresponded to the high amplitude of the negative peak. Since the rising edge of photocurrent is relevant to the pulse duration and has no relationship with the carrier lifetime, the positive peaks of THz radiation under different carrier life-time are basically the same.

Fig. 10(b) is the Fourier-transformed THz spectra of THz radiation. It can be seen that the carrier life-time has almost no influence on the bandwidth of THz radiation, but its central radiation frequency is blue-shifted as the carrier life-time decreases. Therefore, the photoconductive materials with shorter carrier life-time should be selected in practical applications, so that the THz radiation can be extended to higher frequencies.

(a) The peak amplitude of THz radiation

(b) Fourier-transformed THz spectra
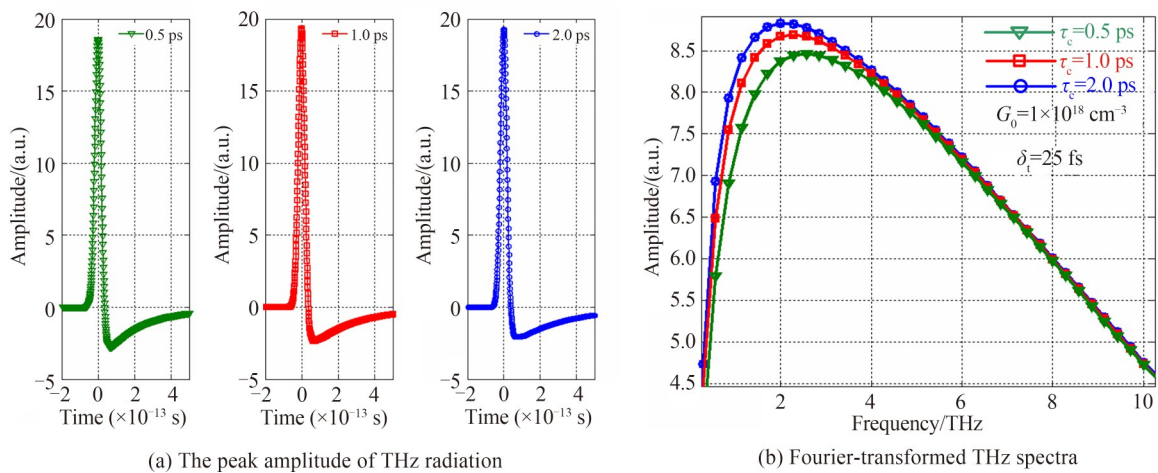
Fig. 10   The relationship between the peak amplitude of THz radiation and the carrier life-time of photoconductor ($\tau_c = 0.5$ ps, 1 ps, and 2 ps)

2.3.2   *Dependence of laser pulse duration*

In this case, the pulse duration of pump laser δ_t is set as the variable. The photocarriers life-time τ_c and the peak generation rate of photocarriers G_0 is set as $= 1$ ps, and $G_0 = 1 \times 10^{18}$ cm^{-3}, respectively.

The relationship between the peak amplitude of THz radiation and the pulse duration of pump laser is depicted in Fig. 11. Figure 11(a) shows the longer pulse duration corresponds to the weaker positive peak power and the stronger negative peak of the THz radiation, while the peak-to-peak amplitudes of THz radiation under different laser pulse durations are almost same. The positive peak power of THz radiation becomes weaker because the photocurrent slowly rises under the pump laser with longer pulse duration, as shown in

Fig. 8. Besides, the absolute negative peak power of THz radiation rises along with the increased pulse duration due to the rapidly dropped photocurrent, as also shown in Fig. 8.

Seen from Fig. 11(b), the longer pulse duration of pump laser corresponds to the narrower THz radiation in frequency-domain. In conclusion, the pulse duration of pump laser can affect the bandwidth of generated THz waves, but the central frequency still remains the same. Therefore, the pump laser with short pulse duration is essential in practical applications to generate broadband THz radiation.

(a) The peak amplitude of THz radiation   (b) Fourier-transformed THz spectra
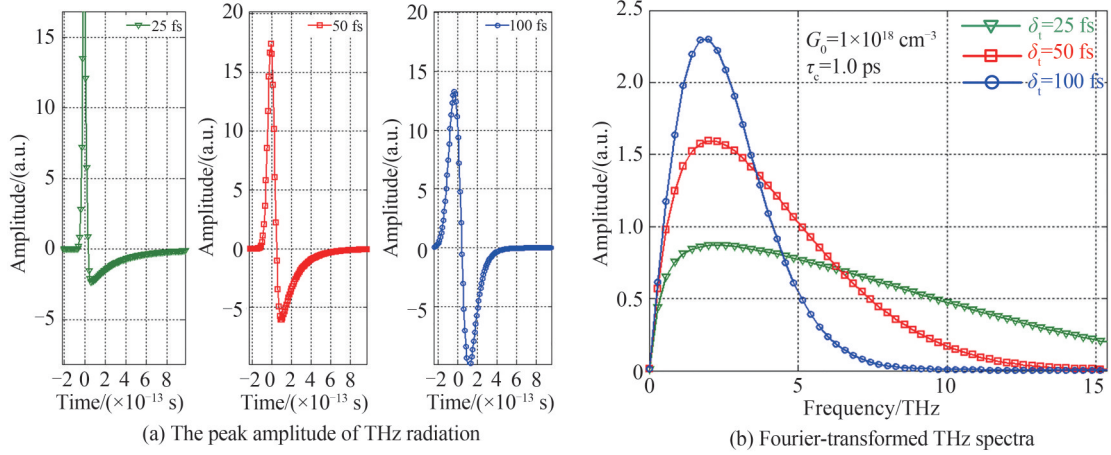
Fig. 11   The relationship between the peak amplitude of THz radiation and the pulse durations of pump laser ($\delta_t = 25$ fs, 50 fs, and 100 fs)

2.3.3 *Dependence of laser peak power*

In this section, the peak carrier generation rate G_0 is set as the variable corresponding to the varied peak power of pump laser. Meanwhile, the life-time of photocarriers τ_c and the pulse duration of pump laser δ_t is set as $\tau_c = 1$ ps, and $\delta_t = 25$ fs, respectively.

The relationship between the peak amplitude of THz radiation and the peak power of pump laser is depicted in Fig. 12. It can be seen from Fig. 12(a) that the peak power of pump laser increases, the amplitude of THz radiation also raises due to the higher carrier density shown in Fig. 4. In addition, the negative part of THz radiation in time-domain becomes more evident under the higher peak power of pump laser due to the increased screening field. Figure 12(b) shows the corresponding Fourier-transformed spectra of THz radiation. It can be seen that the bandwidths in frequency-domain are hardly varied, while the central frequency is blue-shifted with the increased peak power of pump laser. Therefore, below the damage threshold of photoconductor, the highest peak power of pump laser should be employed to generate the strongest photocurrent.

(a) The peak amplitude of THz radiation   (b) Fourier-transformed THz spectra
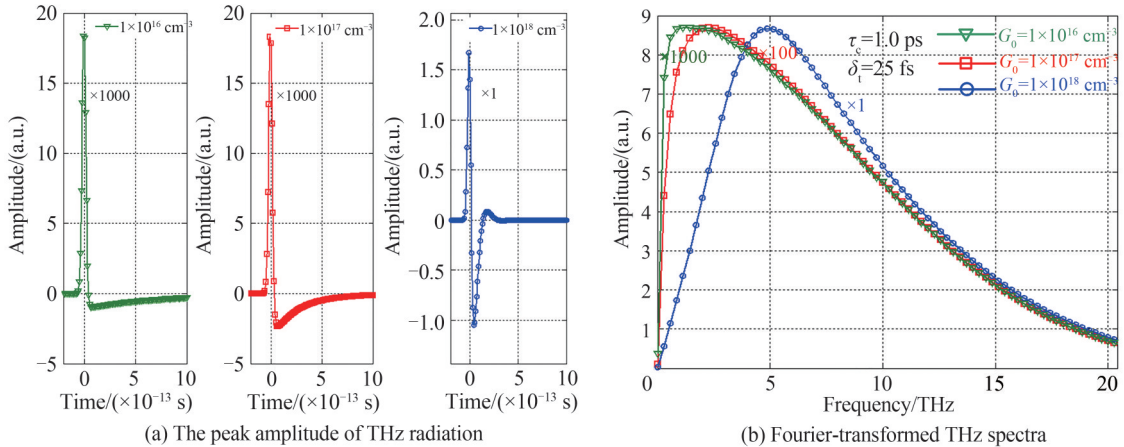
Fig. 12   The relationship between the peak amplitude of THz radiation and the peak pump laser power corresponding to the peak carrier generation rate ($G_0 = 1 \times 10^{16}$ cm^{-3}, 1×10^{17} cm^{-3} and 1×10^{18} cm^{-3})

In summary, the above mentioned simulation reveal the ultrafast dynamics of THz waves generated by THz-PCA, and provide a theoretical basis for generating high-power, broadband THz radiation.

3　Physical mechanism of THz-PCA detector

The detection of pulsed THz waves can also be achieved by THz-PCA with the similar structure of THz emitter [46], as shown in Fig. 13. The probe laser to excite the THz-PCA detector is a portion of the femtosecond laser, synchronized to the pump laser employed for THz waves generation. In contrast to THz-PCA emitter, the biased field is not required for THz-PCA detector. The electric field utilized to drive photocarriers in the photoconductor is offered by the received THz pulse that arrives in synchronism with the probe laser pulse.
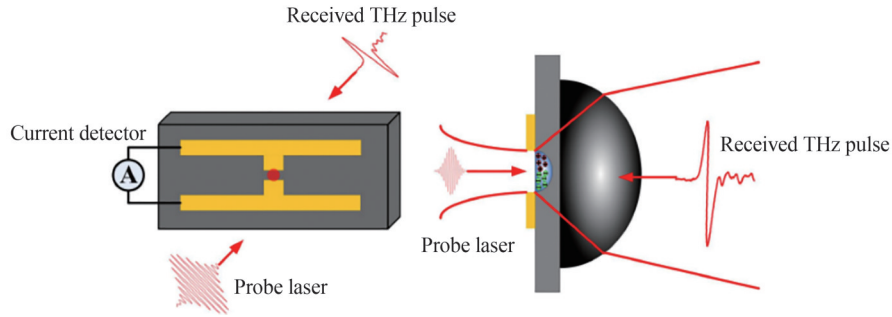
Fig. 13　Schematic of coherent detection on THz waves by THz-PCA

The excited photocarriers are driven by the received THz field E_{THz} to generate a transient photocurrent $J(t)$, which is a convolution of the E_{THz} defined as [42, 47]

$$J(t) \propto \int_{-\infty}^{t} \sigma_s(t-t') E_{\mathrm{THz}}(t') \mathrm{d}t' \tag{10}$$

where $\sigma_s(t)$ is the transient surface photoconductivity of THz-PCA detector.

According to the convolution operation and the Fourier transform, the transient current $J(\nu)$ can be described as

$$J(v) = \sigma_s(v) E_{\mathrm{THz}}(v) \tag{11}$$

where $J(\nu)$, $\sigma_s(\nu)$ and $E_{\mathrm{THz}}(\nu)$ are the Fourier transform of $J(t)$, $\sigma_s(t)$ and $E_{\mathrm{THz}}(t)$, respectively.

Equation (11) indicates that the detection bandwidth of THz-PCA detector is mainly limited by the ultrafast dynamics of carrier in the photoconductor. Moreover, the frequency distortion is inevitable in the received THz signal due to the varied transient surface photoconductivity of THz-PCA detector, which is related to carrier mobility $\mu(t)$, current density $n(t)$, and optical intensity of probe laser $I_{\mathrm{opt}}(t)$.

The carrier mobility is defined as

$$\mu(t, t') = \mu_e \left[1 - \mathrm{e}^{-(t-t')/\tau_s}\right] \tag{12}$$

where μ_e is the electron mobility at steady state and τ_s is the relaxation time of photocarriers.

While the carrier density in the photoconductor decays exponentially, which can be expressed as

$$n(t, t') = \mathrm{e}^{-(t-t')/\tau_c} \tag{13}$$

where τ_c is the carrier life-time.

Considering the incident probe laser in a Gaussian profile, the corresponding incident laser intensity can be described as

$$I_{\mathrm{opt}}(t) = I_0 \mathrm{e}^{-t^2/\tau_p^2} \tag{14}$$

where I_0 is the peak intensity of probe laser and τ_p is the pulse duration of probe laser.

The transient surface photoconductivity of THz-PCA detector can be defined as [48]

$$\sigma_s(t) = \sigma_0 \left\{ \mathrm{e}^{-\frac{t}{\tau_c} + \frac{1}{4}\left(\frac{\tau_p}{\tau_c}\right)^2} \left[1 + \mathrm{erf}\left(\frac{t}{\tau_p} - \frac{1}{2}\frac{\tau_p}{\tau_c}\right)\right] - \mathrm{e}^{-\left(\frac{1}{\tau_c} + \frac{1}{\tau_s}\right)t + \frac{1}{4}\left(\frac{\tau_p}{\tau_c} + \frac{\tau_p}{\tau_s}\right)^2} \left[1 + \mathrm{erf}\left(\frac{t}{\tau_p} - \frac{1}{2}\left(\frac{\tau_p}{\tau_c} + \frac{\tau_p}{\tau_s}\right)\right)\right] \right\} \tag{15}$$

Finally, substituting Eq. (15) into Eq. (10), the time-domain spectrum and its Fourier-transformed spectrum of THz signal measured by THz-PCA detector can be obtained. The characteristics of the surface photoconductivity of THz-PCA detector under different conditions as pulse duration and carrier life-time are investigated as follows, which provides a theoretical method for accurate analysis the ultrafast process of THz waves measured by THz-PCA detector.

3.1 Dependence of probe laser pulse duration

The relationship between the surface photoconductivity of THz-PCA detector and the pulse duration of probe laser (with the fixed carrier life-time $\tau_c = 0.1$ ps and the fixed relaxation time of photocarriers $\tau_s = 30$ fs) is depicted in Fig. 14. Seen from Fig. 14 (a), it is clear that the probe laser with shorter pulse duration corresponds to the higher peak amplitude of $\sigma_s(t)$ and the faster decay time due to the quicker responses of the photocarriers. However, the peak amplitude and the decay time of $\sigma_s(t)$ tend to stable when the pulse duration is less than 25 fs due to the minimum response time of photocarriers. When the pulse duration of probe laser is smaller than the minimum response time, the photocarriers will reach the response limited, indicating a relatively stable value of $\sigma_s(t)$.

(a) Surface photoconductivity

(b) Fourier-transformed THz spectra
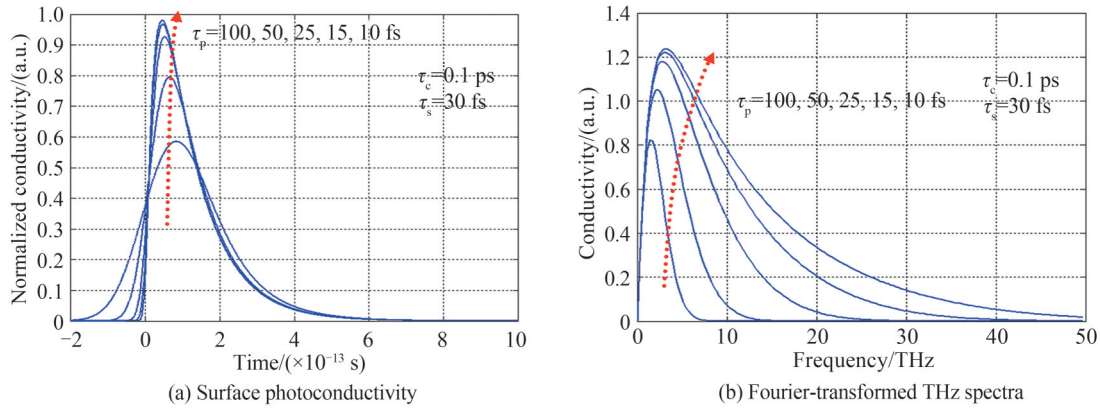
Fig. 14   The relationship between the surface photoconductivity of THz-PCA detector and the pulse duration of probe laser ($\tau_p = 10$ fs, 15 fs, 25 fs, 50 fs, and 100 fs)

Meanwhile, the pulse duration of probe laser has a great influence on the bandwidth of the frequency-domain spectrum of $\sigma_s(t)$, as shown in Fig. 14 (b). The shorter pulse duration corresponds to the broader frequency-domain spectrum. It can be deduced from the spectral response of the $\sigma_s(t)$ that the THz-PCA detector has the characteristics of frequency selection (filtering effect) when it is utilized to detect THz signal, namely, the receiving efficiency of THz-PCA detector depends on the spectrum of the surface photoconductivity and also the spectrum of the THz pulse itself.

The measured THz signal of THz-PCA detector is depicted in Fig. 15, and the red curve is the received THz signal which is emitted by the THz-PCA emitter at far-field condition. For clear distinction, the τ_{pd} and τ_{pe} is the pulse duration of probe laser (for THz detection) and pump laser (for THz generation), respectively. In this simulation, the fixed carrier life-time and the pulse duration of pump laser is $\tau_c = 0.5$ ps and $\tau_{pe} = 25$ fs, respectively.

Due to the screening field occurred in both THz generation and detection, the time-domain waveform of detected THz signal is not fully identical with the actual waveform of received THz signal. Specifically, the negative part of the detected THz signal is larger than that of the received THz signal, as depicted in Fig. 15 (a). Moreover, the shorter pulse duration of probe laser corresponds to the detected THz signal with smaller positive peak amplitude, larger negative peak amplitude and narrower bandwidth. From Fig. 15(b), the characteristics of detected THz signal by THz-PCA detector is completely different under the varied pulse duration of probe laser and the one with shorter τ_{pd} is closer to the received THz signal. Therefore, the THz-PCA detector should utilize a probe laser with short pulse duration to recover the received THz signal as much as possible.

(a) The detected THz signals

(b) Fourier-transformed THz spectra
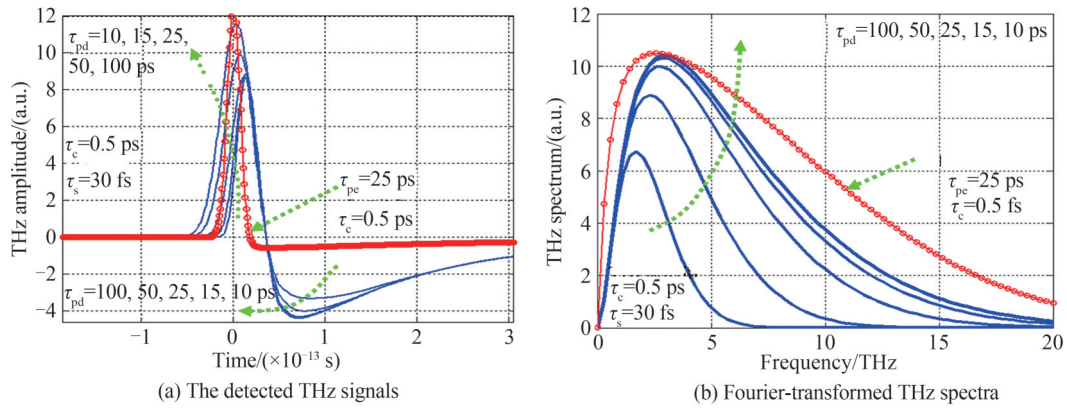
Fig. 15   The relationship between the detected THz signals and the pulse duration of probe laser ($\tau_{pd} = 10$ fs, 15 fs, 25 fs, 50 fs, and 100 fs) and the red curve is the received THz signal

3.2   Dependence of photocarrier life-time

The photocarrier life-time can also affect the surface photoconductivity of THz-PCA detector, which is one of the most important factors for THz detection via THz-PCA. Here, the relaxation time of photocarriers and the pulse duration of pump laser is fixed as $\tau_s = 30$ fs and $\tau_p = 10$ fs, respectively. Figure 16(a) depicts $\sigma_s(t)$ in time-domain with different carrier life-times of the photoconductors illuminated by probe laser. The results are similar to that of the generated carrier density and photocurrent in THz-PCA emitter discussed in Sections 2.1.3 and 2.2.1 previously. Namely, the photoconductor with the longer carrier life-time corresponds to the higher amplitude and broader bandwidth of $\sigma_s(t)$ in time-domain. Seen from Fig. 16(b), the carrier life-time is almost no influence on bandwidth of the $\sigma_s(\nu)$ in frequency-domain, while the central frequency is blue-shifted and the amplitude is decreased with the declined carrier life-time. In one word, the photoconductor with shorter carrier life-time is more preferable to detect the THz signal at higher frequency.

(a) Surface photoconductivity

(b) Fourier-transformed THz spectra
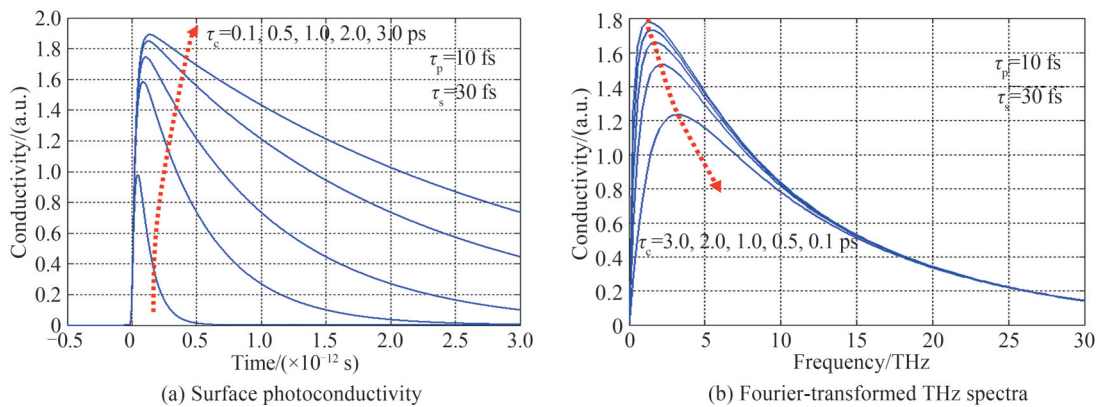
Fig. 16   The relationship between the surface photoconductivity of THz-PCA detector and the carrier life-time ($\tau_c = 0.1$ ps, 0.5 ps, 1.0 ps, 2.0 ps, and 3.0 ps)

The time-domain profiles and its Fourier-transformed THz spectra of detected THz signals are shown in Fig. 17 and the red curve is the received THz signal, which is emitted by the THz-PCA emitter at far-field condition. For clear distinction, the τ_{pd} and τ_{pe} is the pulse duration of probe laser (for THz detection) and pump laser (for THz generation), respectively. In this simulation, the carrier life-time of the THz-PCA emitter, the pulse duration of probe laser and pump laser is fixed as $\tau_c = 0.5$ ps, $\tau_{pd} = 10$ fs and $\tau_{pe} = 25$ fs, respectively.

As can be seen from Fig. 17(a), the time-domain bandwidth of detected THz signal is broader than that of the received THz signal. Therefore, the frequency-domain bandwidth of the detected THz signal is narrower than that of the received THz signal due to the "filtering" effect, as depicted in Fig. 17(b). Moreover, the carrier life-time does not influence on the bandwidth of detected THz signal, but it will affect the spectral response of THz-PCA detector and cause the frequency "distortion". The shorter carrier life-time corresponds

to the higher the central frequency. Under the same conditions, the THz-PCA detector with short carrier life-time can receive more information of high frequency THz signals to broaden the detection range. Therefore, the photoconductive material with short carrier life-time should be selected as the photoconductor of THz-PCA detector to achieve the relatively accurate detection of received THz signal.

(a) The detected THz signals (b) Fourier-transformed THz spectra
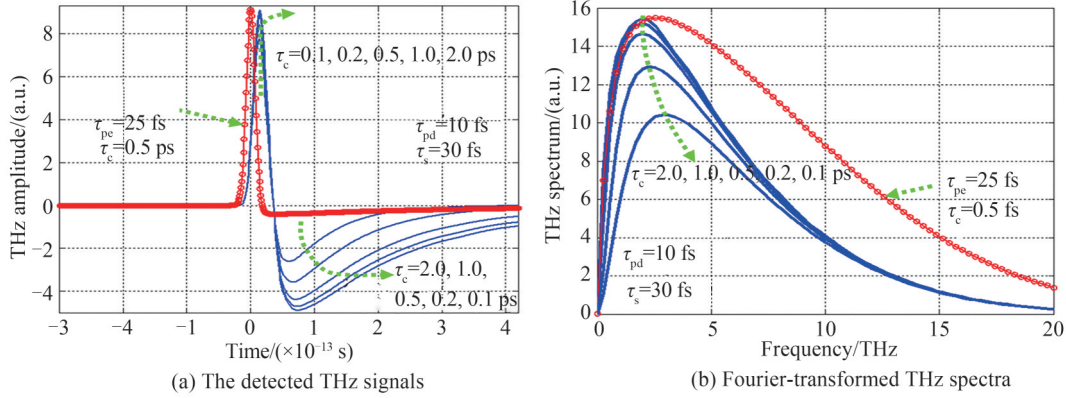
Fig. 17   The relationship between the detected THz signals and the carrier life-times ($\tau_c = 0.1$ ps, 0.2 ps, 0.5 ps, 1.0 ps, and 2.0 ps) and the red curve is the received THz signal

4   Research progress of THz-PCA

After development over four decades, a variety of THz-PCAs are commercially available and become indispensable in many practical applications. Moreover, a plenty of valuable research schemes have been proposed to develop the THz technologies based on THz-PCA including photoconductive materials and structure design of THz-PCA, which are summarized in this section.

4.1   Photoconductive materials

The drift photocarriers within sub-picosecond timescale is one of the most crucial factors to generate or detect the transient photocurrent corresponding to THz frequency range, which requires a photo-absorbing semiconductor with sub-picosecond carrier lifetime [8]. The key to realize sub-picosecond carrier life-time is to shorter the recombination time, namely, introduce a numerous of defects, dislocations and scattering centers in the photoconductor, which can be treated as "inferior quality" semiconductor. Meanwhile, the crystalline properties of photoconductor still need to be maintained for generating the photocarriers with high mobility [9].

For the THz-PCA operating around 800 nm wavelength, GaAs is the most preferable photoconductor since its room temperature bandgap ($E_g = 1.424$ eV) is compatible with the Ti^{3+} : sapphire femtosecond laser. In fact, three types of GaAs, namely, low-temperature-grown GaAs (LTG-GaAs), semi-insulating GaAs (SI-GaAs), and ion-implanted GaAs (GaAs:N^{3-} or GaAs:As^{3+}), have been commonly used in THz-PCA[43,50-51]. However, previous research found that the THz-PCA made by LTG-GaAs exhibited greater performances than that of the SI-GaAs and GaAs:As^{3+} due to the relatively short carrier lifetime [52]. Therefore, LTG-GaAs rapidly becomes the ideal substrate for THz-PCA working around 800 nm wavelength.

The indium gallium arsenide ($In_xGa_{1-x}As$), which has the bandgap ($E_g = 0.8$ eV) compatible with the 1.55 μm excitation, has also been investigated as a potential candidate for the photoconductor of THz-PCA. The main reason to employ 1.55 μm excitation is the easy implementation in practical applications. The pulsed laser system operating around 1.55 μm wavelength can be completely fiber-based [53], thereby the size of THz systems based on THz-PCA with 1.55 μm excitation can be greatly miniaturized. However, the $In_xGa_{1-x}As$ with short photocarriers life-time is quite difficult to be achieved. Different from LTG-GaAs, the $In_xGa_{1-x}As$ grown at low temperature doesn't have shorter carrier recombination time and deeper trap levels [54], thus it is not favorable for efficient THz generation and detection around 1.55 μm wavelength.

There are two promising alternatives to solve this challenge. Firstly, a superlattice of LTG-InGa(Al)As layers can provide the short carrier lifetime around 1.55 μm wavelength. In specific, the incident pulsed laser with 1.55 μm wavelength is absorbed by the InGaAs layer, while the InAlAs can provide the deep

recombination sites to decrease the carrier lifetime [55]. Another method for the 1.55 μm excitation is ion-implanted InGaAs（e. g., InGaAs：Fe²⁺），which can provide the effective recombination sites for sub-picosecond carrier lifetime [56].

Moreover，other group Ⅲ－Ⅴ materials have also been investigated，including InSb，GaAsSb，GaSb，and GaInSb [57, 58-60]. Although more investigations are required to further understand the growth conditions of these materials，the higher operation thresholds compared to GaAs and $In_xGa_{1-x}As$ have been pursuing for the tempting enhancement of THz-PCA performance. Here，the features and key performance of these photoconductive materials reported are summarized in Table 1.

Table 1　The typical photoconductive materials

Materials	Advantages	Disadvantages	Key performance reported
GaAs	800 nm excitation；mature processing technology	Poor absorption at 1.55 μm	10^4 Signal-To-Noise（SNR）in THz detection [61]；60 kV/cm break threshold [62]；0.25 ps carrier lifetime [63]；1.5 times enhancement of THz radiation power [64]
InGaAs	1.55 μm excitation；fiber based laser system	Relatively long carrier lifetime	125 SNR in THz detection [65]；$<$ 5 ps recombination time of carriers [66]；860 μW THz average power [67]
InGa(Al)As heterostructures	1.55 μm excitation；short carrier life-time	Complex material growth	10^3 SNR in THz detection [55]；6 THz bandwidth in THz generation [68]；1 V/cm THz amplitude with 4 THz bandwidth in THz generation [69]
Other group Ⅲ－Ⅴ	High operation threshold	Under developing	1 THz bandwidth and 10^2 SNR in THz detection [57]

4.2　Structure design of THz-PCA

4.2.1　Conventional THz-PCA

During the early stage，the investigation on THz-PCA was mainly focused on the saturation effect at high pump power，which is one of the major factors for restricting the efficiency of THz-PCA. It is well known that the illumination of photoconductor can generate photocarriers to increase total carrier density. When the optical power of pump laser is high enough，the generated photocarrier density can exceed the intrinsic carrier density and the imaginary part of the permittivity of the photoconductor will begin to increase，resulting in the nonlinear raise of the surface reflectivity at the interface between air and photoconductor[70]. Therefore，the output power of generated THz radiation will experience a nonlinear increase，and finally reach a saturation point in which the output THz power can no longer increase even with much stronger pump laser. Of course，the saturation effect of THz-PCA is easier to be seen when the pump laser is focused to a smaller spot size [44].

In order to overcome the saturation limitations of THz-PCA，many approaches have been developed including large aperture dipoles，dipole arrays and interdigitated electrodes. In specific，due to large areas of the large aperture dipoles and the dipole arrays，the pump laser with large spot size can be utilized as the excitation source [71,73]. Moreover，the interdigitated electrodes consisted of interdigitated anode microstrips and cathode microstrips can provide large active areas，allowing the optical power spread over the larger area [75-76]. These devices can effectively reduce the saturation effect at higher pump power，which is crucial for high output power of THz-PCA. Some major progresses are summarized in Table 2.

Moreover，it is worth to point that Upadhya and Fan et al. have found that the asymmetrically excited THz-PCA with smaller spot size，where the position of pump laser is close to the anode，has better performances in bandwidth and intensity of generated THz wavs [80]. However，the underlying physical mechanism is still unclear until the THz-PCA incorporated with plasmonic electrodes has been proposed [49].

Table 2　The Summary of conventional THz-PCAs

Types	Advantages	Disadvantages	Key performance reported
Large aperture dipoles	The saturation effects can be greatly alleviated	High bias field	No saturation effects until the 90 μW/cm² of optical fluence [71]; 4 times enhancement of THz radiation power [72]
Dipole arrays		The complexity in optical alignment	1.9 mW THz radiation power [73]. Detect the polarization state of THz waves [74]
Interdigitated electrodes		The complex fabrication and design process	15~85 V/cm radiated THz field [75-76]; > 80 kV/cm radiated THz field [77]; 6 times enhancement of maximum detected THz intensity [78]; Average THz radiated power of 3.956 4 mW [79]

4.2.2　THz-PCA with plasmonic nanostructures

In general, the drift velocity of photocarriers in the semiconductor is a certain value, and thus the maximum transport distance of the photocarriers before their recombination can be obtained. For instance, the maximum drift velocity and lifetime of photocarriers in LTG-GaAs are $v = 10^7$ cm/s and $\tau_c = 1$ ps, respectively. Therefore, the maximum transport distance of the photocarriers in LTG-GaAs is

$$d = v \times \tau_c = 10^5 \times 10^{-12}\,\mathrm{m} = 100\,\mathrm{nm} \tag{16}$$

This indicates only the photocarriers within transport distance of around 100 nm near the antenna anode can be made real contribution to the transient photocurrent. Consequently, the fractions of photocarriers that can reach the metal electrodes directly decide the quantum efficiency of THz-PCA.

In order to realize the THz-PCA with high operation efficiency, the percentage of generated photocarriers that arrive at the metal electrodes in sub-picosecond time-scale should be as much as possible. However, only a very small percentage of the incident photons can be absorbed near the photoconductor surface, not to mention the number of excited photocarriers near the electrodes to be collected on a sub-picosecond time-scale [49]. This restriction has severely hindered the enhancement of radiation power output from THz-PCA emitter, as well as the sensitivity and response frequency range of THz-PCA detector.

Fortunately, the development of plasmonic nanostructures greatly improves the performances of THz-PCAs. The plasmonic nanostructures can be delicately engineered to remarkably enhance the optical absorption in the active area of photoconductor and the transport distance can also be reduced due to its strong field localization. Surface Plasmons (SPs) are collective oscillations of electron-plasma existed at the metal-dielectric interface [8,81], which has been proved to be a promising method for improving the operation efficiency for both THz-PCA emitter and detector [8,49]. Generally, there are four types of plasmonic nanostructures employed to enhance the performances of THz-PCA, namely, plasmonic light concentrators, plasmonic contact electrodes, optical nanoantenna arrays, and optical nanocavities, as shown in Fig. 18. Their characteristics and disadvantages are discussed as follows, and the key performances reported are summarized in Table 3.

Plasmonic light concentrators, shown in Fig. 18(a), are metal nanostructures located between the metal electrodes for exciting the SP waves at operation wavelengths that are tightly restricted at the interface of metal-photoconductor [82]. Accordingly, the optical absorption near the plasmonic light concentrators can be significantly enhanced; thereby the generated photocarriers density in the active area of photoconductor can also be improved. Eventually, more photocarriers can reach the metal electrodes in the sub-picosecond time-scale to produce the transient photocurrent. However, the relatively long transport distance of photocarriers is still a problem that needs to be settled.

Plasmonic contact electrode, as depicted in Fig. 18(b), is also a promising method to improve the operation efficiency of both THz-PCA emitter and detector [49]. In addition to having the advantages similar to plasmonic light concentrators, plasmonic contact electrodes can also greatly reduce the transport distance of the photocarriers because they are directly connected to the metal electrodes. Therefore, the THz-PCA with plasmonic contact electrodes can prompt more photocarriers to reach the metal electrodes in the sub-picosecond time-scale than that of the THz-PCA with plasmonic light concentrators, and thus its operation efficiency can be further improved.

(a) Plasmonic light concentrators (b) Plasmonic contact electrodes

(c) Optical nanoantenna arrays (d) Optical nanocavities
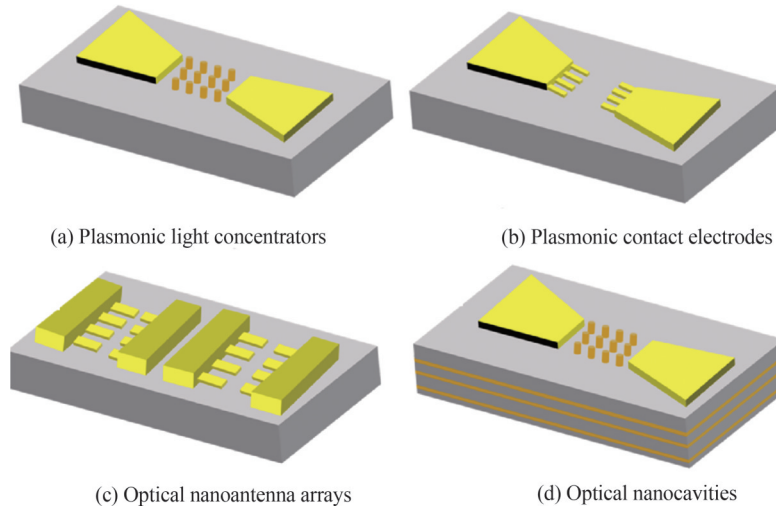
Fig. 18 The THz-PCA incorporated with plasmonic nanostructures

Table 3 The development of THz-PCA incorporated with plasmonic nanostructures

Types	Key performance reported
Plasmonic light concentrators	2.4 times enhancement of THz radiation power [82]; 20 dB enhancement of THz radiation power [83]; 5.6 times enhancement of THz radiation power [84]
Plasmonic contact electrodes	50 times enhancement of THz radiation power [49]; 30 times enhancement of THz detection sensitivity [49]; 7.5% optical-to-THz conversion efficiency in THz generation [85]; 40 times enhancement of output photocurrent in THz detection [86]; 17 μW radiation power at 1 THz [87]; THz detection with quantum-level sensitivity at room temperature [88]; $\sim$ 138 times enhancement of THz radiation power [89]
Optical nanoantenna arrays	THz radiation power of 3.8 mW over $0.1 \sim 5.0$ THz [90]; 300 μW THz radiation power over $0.1 \sim 5.0$ THz [91]; 107 dB SNR over $0.1 \sim 4.0$ THz in THz detection [92]; 95 dB SNR over a 4.0 THz bandwidth in THz detection [93]
Optical nanocavities	80%$\sim$85% absorption of the incident pump laser for PCA detector [94]; 4 mW THz radiation power over $0.1 \sim 4.0$ THz [95]

Similar to the aforementioned conventional THz-PCA in Section 4.2.1, the saturation effect also exists and become more evident due to the enhanced local electric field in THz-PCA with plasmonic nanostructures [8]. Therefore, the optical nanoantenna arrays, as shown in Fig. 18(c), have also been proposed to address this obstacle [90-92]. Due to the large area of this type of THz-PCA, the pump laser with large spot size can be employed for illumination and alleviate the screening effect. Therefore, higher optical power of the pump laser and higher bias field can be implemented.

In order to further confine the generated photocarriers in a small volume near the metal electrodes, the optical nanocavities have been proposed and detailly investigated [94-95]. The optical cavity is consisted of a plasmonic nanostructure array on the top side of photoconductor and a Distributed Bragg Reflector (DBR) on the bottom side, as shown in Fig. 18(d). The plasmonic nanostructure array is designed to reduce the optical reflection within the stop band of the DBR to confine the incident photons near the metal electrodes. This design can significantly improve the optical absorption of the active layer in photoconductor, which is extremely critical for photocarriers generation. Although the THz-PCAs with optical nanoantenna arrays or optical nanocavities are more efficient than others, the complex machining process and structural design has still hindered their practical applications.

In general, the plasmonic nanostructures (e.g., nanodisk and nanograting) are the most important factors for improving the performance of THz-PCA. Therefore, some important structural parameters are summarized as follows. The typical gold light concentrators with operation wavelength of 800 nm have the periodicity of 420 nm, diameter of 230 nm and height of 120 nm in Ref. [84]. It is worth to note that the transport distance of photocarriers is 100 nm according to Eq. (16), indicating that the gap width between the plasmonic contact electrodes should be less than 100 nm to improve the utilization of the photocarriers. In Ref. [49], a typical gold grating with operation wavelength of 800 nm have the 200 nm pitch, 100 nm gap width and 50 nm height.

4.2.3 *THz-PCA with all-dielectric nanostructures*

The ohmic loss and heat transfer of plasmonic nanostructures still remains a challenge to be solved, because they may lead to the damage of THz-PCA under strong optical excitation or high bias voltage as well as the deterioration of carrier screening effect [47]. As an example, the THz-PCA embedded with plasmonic nanostructures in Ref. [96] theoretically claims a 335 times enhancement of transient photocurrent, while the experimental result indicates only a 10.6-time improvement due to the deteriorated carrier screening effect.

Therefore, the all-dielectric nanostructures composed of Mie resonators has attracted more attention in recent years and have also been considered as a promising alternative to plasmonic nanostructures, including all-dielectric gratings and all-dielectric metasurfaces, which can also realize the reducing of optical reflection. It is worth to note that the insufficient electric field enhancement of all-dielectric nanostructures cannot confine the photocarriers in a small volume [97]; thereby the current performances reported are less than that of the THz-PCAs with plasmonic nanostructure. The key performances of THz-PCA incorporated with all-dielectric nanostructures reported are summarized in Table 4.

Table 4 The development of THz-PCA incorporated with all-dielectric nanostructures

Types	Key performance reported
All-dielectric gratings	70% enhancement of THz radiation power (simulation) [98]; 10^6 SNR in THz detection over 0.1~4.0 THz [99]; 3 times enhancement of THz radiation power [100]; 3.92 times enhancement of THz radiation power [101]
All-dielectric metasurfaces	6-time enhancement of SNR in THz detection over 0.1~1.1 THz [102]; 10^6 THz-TDS dynamic range at 5 μW excitation [103]
Topological insulator	60 dB dynamic operation range [104]
Si quantum dots	~880 times enhancement of THz detection sensitivity [105]

4.2.4 *Some work on THz-PCA in our group*

Our group has also carried out numerous investigations relevant to the THz-PCA, including theoretical analysis and simulation, optimized structural design of PCA and nanostructures, experimental demonstrations, and practical applications in THz-TDS. The theoretical analysis has been summarized in Section 2 and 3, and the practical applications in THz-TDS are exhibited in Sections 5 and 6 in detail, while the others are summarized in this section.

Since the antenna gap has important impacts on THz wave generation, we firstly simulated the two-dimensional (2D) and three-dimensional (3D) distributions of electric fields between the antenna anode and cathode, as depicted in Figs. 19(a) and (c), which provide a theoretical guidance for the illuminated optical power and the applied bias field. Moreover, the metal electrodes may be injured under the thermal effect from the illumination of femtosecond laser. Therefore, the distributions of electric fields between the antenna anode and cathode from the injured THz-PCA have also been simulated and depicted in Figs. 19(b) and (d). It is clear that the electric field around the injured electrodes is weaker than that around the non-injured electrodes, which will decrease the radiation power of generated THz waves. And also, this has been demonstrated by our experimental results [106].

For our home-made THz-PCAs, the LTG-GaAs was selected as the photoconductor due to its short carrier lifetime and the metal electrodes were made by Au/Ni. The geometrical shape of antenna is the optimized parallel plate electrode with gap size of 800 μm and 20 μm, respectively. And the picture of THz-

(a) THz-PCA without injury (2D) (b) THz-PCA with injury (2D)

(c) THz-PCA without injury (3D) (d) THz-PCA with injury (3D)
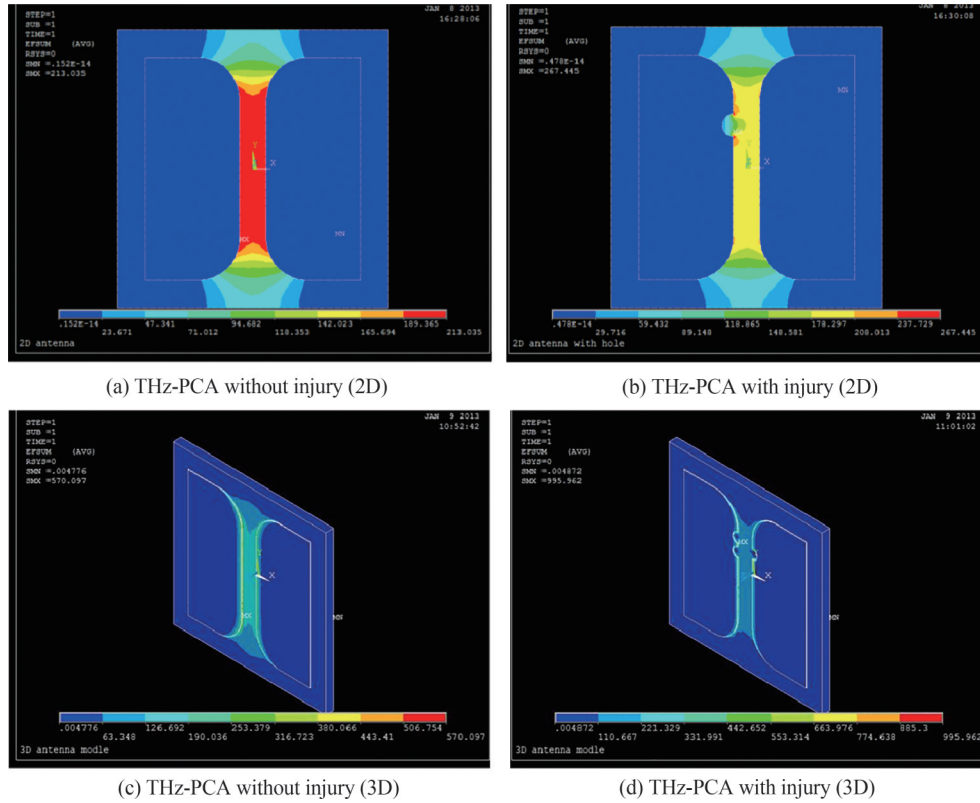
Fig. 19　The simulation of THz-PCA without and with injury

PCAs are depicted in Fig. 20. It is worth to point that our designed THz-PCAs have the metal electrodes with the circular arc instead of the square edge, which can effectively prevent discharge from the sharp corner of the metal electrodes and protect the THz-PCA from electric field breakdown [83].

The experimental results of our designed THz-PCAs are shown in Fig. 21. In our experiment, the average power of incident femtosecond laser was set as 20 mW, and the applied bias voltage was ± 50 V. It is clear that the time-domain peak THz amplitude of large aperture THz-PCA is almost 2 times higher than that of small aperture THz-PCA because the gap size of small aperture THz-PCA is much small than the spot size of the pump laser. The experimental results shown in Fig. 21 demonstrate that the two typical home-made THz-PCAs can generate THz waves at low excitation power (20 mW). However, the radiation intensity and frequency domain characteristics are mainly limited by the characteristics of photoconductive materials, antenna shape, gap size, and laser power density as well as the laser pulse duration.

Besides, the influences of the laser spot size focused on the THz-PCA emitter were also experimentally investigated [107]. In our experiment, a mode-locked Ti: Sapphire laser with a central wavelength of 790 nm was employed to excite the THz-PCA emitter. The laser beam is split into pump laser and probe laser by a splitter. The pump laser is focused onto the THz-PCA for generating THz waves, which are collimated and focused by parabolic mirrors. After interaction with a ZnTe crystal, the generated THz signals are transmitted from a home-made differential detector to a lock-in amplifier, and then sent to the computer for analysis.

According to the experimental results, we have found that the pump laser with smaller spot size corresponds to stronger THz radiation power. However, the intensity of THz radiation cannot be further enhanced while the optical intensity of laser power reaches a certain value, and this saturation effect has been detailly analyzed in Section 4.2.1. Eventually, by optimizing the optical reflector, applied bias field and modulation frequency, the coverage of THz signal in frequency-domain can be extended from 2 THz to more than 4 THz, and the peak-to-peak amplitude of the time-domain signal is also increased by 50%.

Moreover, we have designed the plasmonic electrodes incorporated with the THz-PCA. The optimized parameters are depicted in the Fig. 22(b): the width of Au gratings is 40 μm, the gap between Au gratings is 100 μm, the thickness of the Au gratings is 95 nm, and the thickness of passivation layer (Si_3N_4) is 245 nm.

(a) THz-PCA with large aperture   (b) THz-PCA with large aperture

20 μm

(c) The detailed view of small aperture THz-PCA

Fig. 20   The view of home-made THz-PCAs

(a) The results of large aperture THz-PCA   (b) The results of small aperture THz-PCA
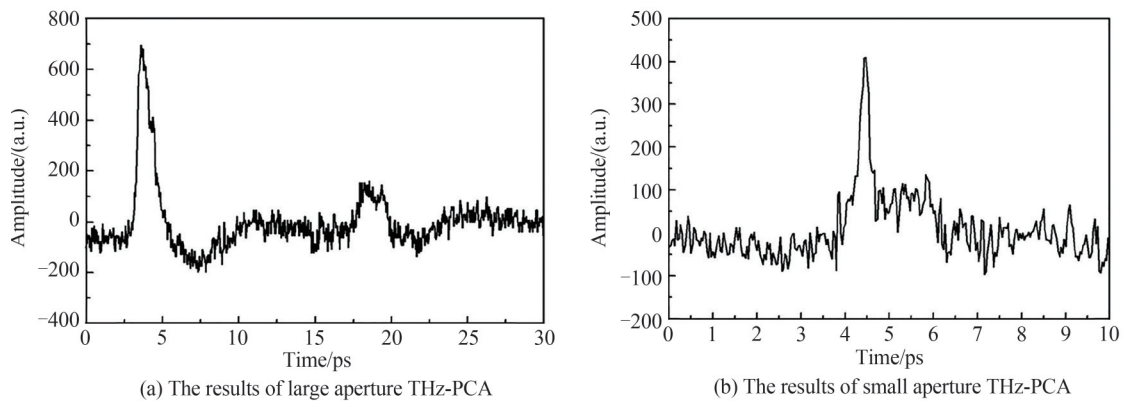
Fig. 21   The experimental results of our designed THz-PCA

The optical transmission of 800-nm-pump laser can reach to 100%, as shown in Fig. 22(a). Moreover, the electric field distributions in the photoconductor depicted in Fig. 22 (b) indicate the remarkable field enhancement near the plasmonic gratings. The above mentioned characteristics in our designed plasmonic gratings can not only improve the pump laser transmission to generate more photocarriers, but also enhance the localized electric field near the plasmonic electrodes to reduce the photocarriers transport time. Therefore, the photocurrent can be greatly improved and subsequently enhance the THz radiation power.

For the practical deposition of gold (Au) film (e.g., thermal evaporation), an adhesion layer is normally required for Au electrodes to stick firmly with the photoconductor. Many adhesion layers such as AuGe/Ni, Pd/Ge, Ti/Pt have been introduced to deposit an ohmic contact to lower the energy barrier of the Au-GaAs junction [108-110]. However, these contacts require multiple metal layers beneath the Au electrodes, which

(a) The optical transmission

(b) The electric field distributions
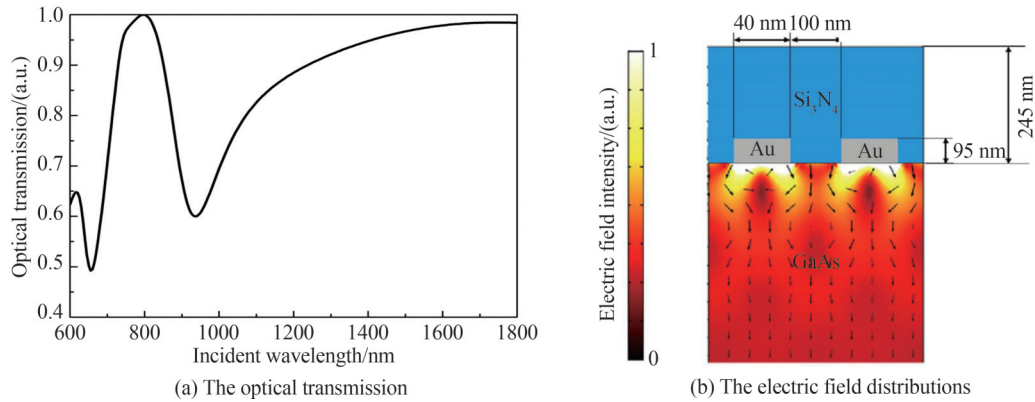
Fig. 22   The optical transmission and the electric field distributions in the photoconductor

increase the distance between the Au and GaAs that decrease the plasmonic enhancement [111]. Therefore, they are not appliable for THz-PCAs with plasmonic nanostructures.

The adhesion layer consisted of Cr and Ti, which can work as a Schottky contact, have also been proposed to address the above mentioned defect [112-113]. Therefore, their optical properties have been investigated and shown in Fig. 23(a), the optical transmission of the plasmonic gratings composed of Cr/Au around 800 nm is 97.5%, while the plasmonic gratings composed of Ti/Au is 97.2%. Therefore, the differences in optical transmission between Cr/Au and Ti/Au can be neglected. However, previous investigations have found that the Cr-GaAs interface has a lower barrier height compared to that of the Ti-GaAs interface due to the Fermi-level pinning effect, which can realize stronger field enhancement [110]. Eventually, Cr is selected as the adhesion layer. Besides, in order to avoid the destructive interference among the generated THz waves, we have also added another metal structure on the top of the passivation layer, which is named as mask layer. Moreover, the optimized parameters of the mask layer are as follows: grating period is 280 nm and the width of Au grating is 140 nm. Finally, the designed THz-PCA is shown in Fig. 23(b).

(a) The optical transmission

(b) The schematic of designed THz-PCA
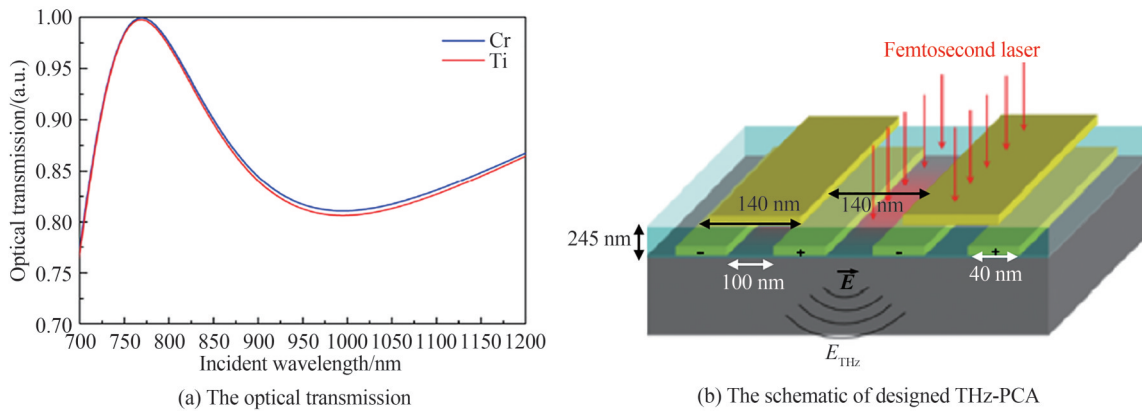
Fig. 23   The optical transmission and the schematic of designed THz-PCA with adhesion layer

Very recently, we have also proposed a THz-PCA with all-dielectric metasurfaces as the antireflection layer and the plasmonic nanostructures embedded in the photoconductor for realizing the field enhancement [97], as shown in Fig. 24(a). The top dielectric metasurfaces can improve the absorption of the incident pump laser in the photoconductor for generating more photocarriers. Meanwhile, the plasmonic nanostructures are able to increase the electrons' drift velocity, namely, confine the electrons near the antenna anode and allow more electrons arriving antenna anode before recombination.

The performances of designed THz-PCA were theoretically analyzed by using a multi-physics model to solve Maxwell's equations, Poisson's equations and drift-diffusion equations. The simulated photocurrent and intensity of radiated THz field are depicted in Figs. 24(b) and (c), respectively. The results indicate that the proposed THz-PCA is 4.9 times higher in photocurrent, and 8.4 times stronger in the intensity of the radiated

THz field than that of the traditional THz-PCA, implying that the designed THz-PCA can greatly promote the THz technology based on THz-PCAs.

(a) The schematic of designed THz-PCA

(b) The simulated photocurrent of THz-PCAs

(c) The simulated THz field intensity of THz-PCAs
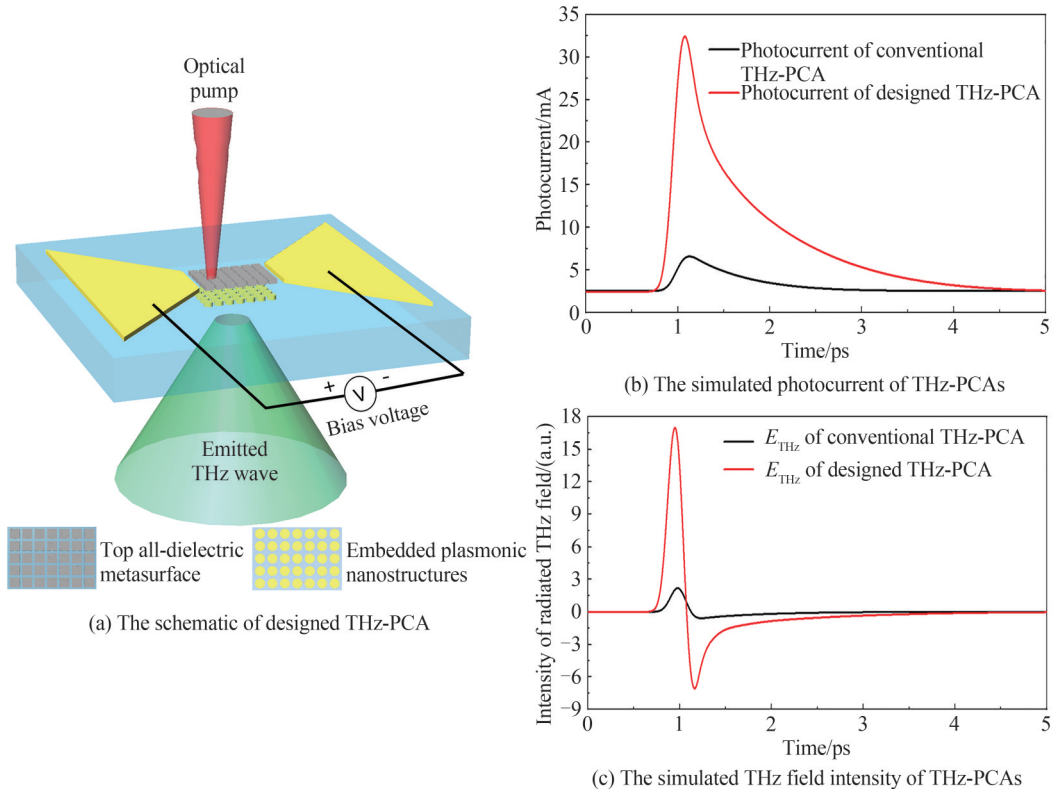
Fig. 24　The schematic and simulation results of designed THz-PCA

5　Terahertz time-domain spectroscopy based on femtosecond laser

5.1　Terahertz time-domain spectroscopy

As an emerging and cutting-edge technology, THz-TDS is the most commonly used technique in current commercial THz spectroscopy [12]. The typical setup of THz-TDS is shown in Fig. 25, which includes a femtosecond laser, delay stage, THz emitter, THz detector and data-acquisition system. Firstly, a pulsed Ti: sapphire laser beam, typically a few hundred milliwatt average power with less than 100 fs pulse duration and around 800 nm center wavelength, is split into pump beam and probe beam by a beam splitter. The pump beam is incident on the THz emitter to generate THz pulses as described above, where the emitter comprises a pair of vacuum-evaporated Cr/Au electrodes separated by a submillimeter-wide gap, fabricated on a LTG-GaAs layer. Then, THz pulses are collimated and focused on the sample using a pair of parabolic mirrors. Finally, the transmitted THz pulses, carrying sample information, are collected and re-focused on the THz detector.
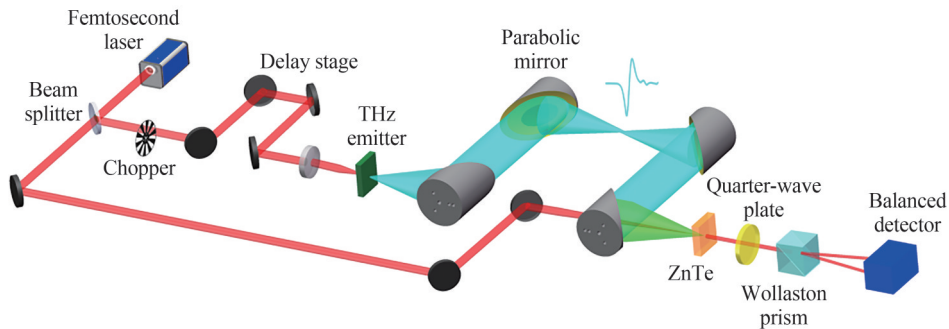
Fig. 25　Schematic diagram of typical THz-TDS system

Detection of the transmitted THz radiation can be achieved by the ultrafast Pockels effect in which the THz beam is collected and focused onto an Electro-Optical Sampling（EOS）detection crystal，such as ＜110＞ ZnTe [114]. When the probe laser pulses and the THz radiation collinearly pass through the electro-optic crystal in a specific crystal orientation，the refractive index ellipsoid of the electro-optic crystal is modulated by THz electric field，causing the polarization direction of the probe laser changed，resulting in the phenomenon of birefringence. And the polarization rotated is proportional to the magnitude of the detected THz electric field. The birefringence modulated the ellipticity of the probe laser beam，which can be measured using a quarter wave plate（$\lambda/4$），a Wollaston Polarization（WP）splitting prism，and two balanced photodetectors. Namely， the modulated probe beam is split into two orthogonal pulses which are passed on to the balanced photo-diode detectors for measurement. A delay stage is used to offset the optical length between the pump and probe laser beams，and finally the THz temporal profile is iteratively sampled by scanning the delay stage. By measuring the signal as a function of the time delay between the THz pulses and the probe laser pulses，the electric field of the THz pulse in time domain can be obtained，and the Fast Fourier transform gives the frequency domain spectrum of THz radiation [115]. Typical THz-TDS system has a frequency bandwidth between 0.1 and 4.0 THz，a spectral resolution of 15 GHz. Signal-processing algorithms can also be used to improve the signal-to-noise ratio of the measured THz signals.

5.2 Advantages of THz spectroscopy technology

5.2.1 *Coherent technique: obtaining refractive index and absorption coefficient directly*

For transmission measurement of THz-TDS，it obtains the time domain signal waveform with the sample information when THz pulse passes through the sample，then Fourier transform gives the frequency domain THz spectrum either as the reference spectrum$A_r(\omega)\exp[-i\phi_r(\omega)]$（without sample）or the signal spectrum$A_s(\omega)\exp[-i\phi_s(\omega)]$（with sample）. The absorption spectrum is proportional to the logarithm ratio of THz spectra taken from sample and reference，respectively. Moreover，the dielectric properties of the sample can be obtained directly by comparing the signal spectrum and reference spectrum without Kramers-Kronig relationship [116]

$$n_s(\omega)=\frac{1}{d_s}\left\{\frac{[\phi_s(\omega)-\phi_r(\omega)]c}{\omega}+n_r d_r\right\} \tag{17}$$

$$\alpha_s(\omega)=\frac{2}{d_s}\left\{\ln\left[\frac{n_s(1+n_r)^2}{\dfrac{A_s(\omega)}{A_r(\omega)}n_r(1+n_s)^2}\right]+\frac{\omega\kappa_r d_r}{c}\right\} \tag{18}$$

where α_s is the absorption coefficient of the sample，n_s is the refractive index，d_s is the thickness of the sample， n_r is the refractive index of the reference medium，d_r is the thickness of the reference medium，κ_r is the extinction coefficient of the reference medium，and c is the speed of light in vacuum.

5.2.2 *Spectral fingerprint*

Unlike local molecular vibrations，such as bending and stretching motion associated with a single chemical bond in the mid-infrared region（$2.5\sim25$ μm，or $4\ 000\sim400$ cm^{-1}），the photon energy of THz wave largely coincides with energy levels corresponding to intermolecular vibrations bonded by hydrogen bonding，van der Waals interactions such as the vibration，rotation，and translation of the molecular skeleton as well as crystalline phonon vibrations. Because of the collective nature of modes in THz spectroscopy，their frequency position and strength are highly sensitive to the conformation and structure of the molecule and its nearby environment. These specific molecular motions can be utilized to distinguish molecules by measuring their characteristic spectral signatures in THz frequency range. Therefore，there has been great interest in applying THz spectroscopy to characterize various materials in past decades and extensive achievements have been accomplished in chemical identification [117-120]，biomedical [121-122]，pharmaceuticals industry [123-124]，composition and conformation monitoring [125-126]. It is now evident that substance can be effectively recognized and characterized according to their distinctive THz fingerprints.

5.2.3 *High temporal—spatial resolution*

THz radiation can be employed to obtain characteristic frequency features with spatial resolution of several micrometers even tens of nanometers by near-field spectroscopic modalities and reveal time-resolved dynamics on the sub-picosecond to picosecond timescales [127-129]. Therefore, THz spectroscopy permits time-resolved investigations of various materials with unprecedented sensing capability, such as carrier dynamics of semiconductor materials [130]. Particularly, by sensitively probing the fast hydration dynamics around biomolecules whose key large-amplitude motions coincidently occur on the picosecond timescale of THz frequencies (1 THz corresponding to 1 ps), THz technology can also be utilized in monitoring intermolecular interactions, including protein hydration and protein-ligand binding [131-132]. THz spectroscopy has been demonstrated unique advantages for detecting the coupling between biomolecules and their hydration shells when it is compared with conventional dielectric spectroscopy, X-ray crystallography, or nuclear magnetic resonance spectroscopy [133].

5.2.4 *Noninvasive and nonionizing properties*

The relatively low-energy of THz photons (4 meV corresponding to 1 THz) in comparison with X-rays makes it suitable for biomedical application without ionization damage. THz wavelengths are longer than infrared and visible light, and scattering losses in biological molecules can be negligible. Moreover, the radiation power obtainable from typical THz-TDS systems is modest and is not considered to pose a health risk. Additionally, an attractive feature of THz spectroscopy is that THz radiation can transmit through many nonmetallic and nonpolar materials, allowing the possible spectral analysis of materials concealed within dry packaging, such as paper, plastics, cardboard, which is favorable for security inspection.

5.3 Metamaterial assisted THz technology for ultrasensitive sensing

THz spectroscopy demonstrates many new potential applications, and shows great promise in molecular fingerprint detection in biomedical and security sensing. However, due to the diffraction of hundreds of micrometer wavelength of THz waves, conventional free-standing spectroscopy usually requires a large amount of sample materials [134]. THz signatures can hardly be captured in microgram level or trace amount, because of the limited power of THz sources, and the low sensitivity of THz detectors. To obtain better sensitivity of THz detections, THz Attenuated Total Reflection (ATR) spectroscopy [135], THz differential time-domain spectroscopy [136], microfluidics [137] and Metamaterials (MMs) [138] are developed. Among them, THz metamaterial sensing is not only signal-enhancing but also easy to be operated, which attracts significant attentions from researchers in extensive fields.

Metamaterials are periodically arranged artificially materials with sub-wavelength features exhibiting many exotic properties, such as super lensing, negative refractive index and perfect absorption. Within the rapid progress in recent decades, the development of metamaterial research lies on diverse aspects that have been reported, such as all-dielectric metamaterials [139], graphene metamaterials [140], reconfigurable metamaterials [141], flexible metamaterials [142], tunable metamaterials [143], and metasurfaces [144]. These MMs are suitable for sensing applications as they can produce spoof surface plasmons [145] with localized electric field enhancement and large values of quality factor (Q factor) [138] which show high sensitivity to minor environmental changes. With the local field enhancement characteristic of MMs and the fingerprint spectral feature of THz waves, THz MMs sensors are highly effective tools for material identification, chemical and biological sensing. For MMs sensors, high Q factor indicates low loss rate, strong light-matter interaction and good sensitivity to environmental change, which is very important and in high demand. Particularly, the Q factor of THz-MMs based on theoretical simulation can be high up to a few thousands [146-147]. In addition, one of the most critical characteristics that determine the performance of MMs sensors is the sensitivity [138], which is also highly dependent on the structure topology optimization of the MMs as well as selection of consisting materials.

Based on elaborate structural design and precise fabrication, many three-dimensional (3D) MM structures have been reported and manifested the strong dipolar response, exhibiting distinctive electromagnetic phenomena of resonant transparency and unconventional optical activity [148-149]. However, the realization of 3D MMs is usually quite challenging due to the restrictions of a sophisticated micromachining technique. Recently, planar THz toroidal-resonant metadevices have been widely studied due to easier fabrication by using conventional photolithography fabrication techniques [144,147,150-151]. The ultrathin thickness in the wave

propagation direction can greatly suppress the undesirable losses caused by the resonant responses and the metallic structures. Therefore, MMs-assisted THz sensing platform has been increasingly implemented for chemical and biological sensing. However, the experimentally measured Q-factor of resonance is somehow very low which is around ten [152-154]. Because the plasmon resonance response of MMs is strongly dependent on structural design and geometric dimensions, designing suitable MMs for highly sensitive THz sensing devices is more related to engineering applications, higher requirements are put forward for fabricated machining accuracy.

6　THz characteristic spectra and application

In fact, THz-TDS provides a new insight into the structural characteristics and mechanism of the spectral responses in molecular level. It is evident that THz spectra represent a characteristic "fingerprint" of a molecular substance, such as important biomolecules, pharmaceutical molecules. On the other hand, with the development of computational chemistry, the assignments of THz spectral features and vibrational modes become more accurate and reliable, even match very well with the THz characteristic spectrum of substance taken from experiments.

6.1　THz spectral analysis-quantum chemical calculation

First principles simulations using quantum chemical calculation methods have been used to interpret the experimental THz spectra, which simulate the physical and chemical properties of substances, such as binding energy, dielectric properties and vibrational spectra, on the basis of the optimal structure of the molecular system based on energy minimum. Since the Schrödinger equation cannot be solved exactly for multi-electron atoms, it is necessary to take approximation methods to obtain the wavefunctions and energies. Hartree-Fock (HF) method can be used to separate the Schrödinger equation into n one-electron hydrogen-like equations for an n electron atom [155], which is typically used for simple molecular systems or preliminary calculations. Moreover, Second-order Møller-Plesset perturbation theory (MP2) based on the Rayleigh-Schrödinger perturbation theory [156], is used for solution-phase spectral analysis or interactions in dimers. Furthermore, Density Functional Theory (DFT) is the most commonly used computational method in THz spectral analysis, which can be utilized to calculate the total electronic energy and the overall electron density distribution [157]. Normally, DFT requires the exchange/correlation functional, the B3LYP [158], B3PW91 [159], PBE [160] and PW91 [161] are the most popular functionals used for DFT calculations. On the other hand, the special DFT approach that uses planewaves in conjunction with pseudopotentials instead of atom-centered basis sets has some advantages for the calculation of solid-state structures with periodic boundary conditions [162].

6.2　THz fingerprinting and chemical identification

6.2.1　Biomolecules: amino acids, nucleobases and saccharides

In recent decades, there have been a great number of studies on applying THz spectroscopy to measure and characterize various biomolecules which reveal a dense set of absorption features in THz range. As shown in Fig. 26, naturally occurring amino acids (alanine, phenylalanine and tyrosine) and nucleobases of cytosine (C) and thymine (T) have distinct absorption features in THz range, and thus, can be clearly distinguished [163]. On the other hand, first principles simulations using quantum chemical methods are utilized to interpret the origin of the experimental THz spectra measured. The intermolecular vibrations are found to be the dominating contributions to the measured spectral peaks of L-alanine in the frequency range of 0.5~4.0 THz [164]. In addition, as shown in Fig. 26(b), all measured THz absorption features of cytosine could be reproduced according to quantum chemical calculations [163]. The results show that absorption features of cytosine below 3.5 THz arise from external modes in translation and rotation motions, which are dominated by the intermolecular hydrogen bonds. The intrinsic absorptions by biomolecules originate from the hydrogen bonds and non-bonded interactions are sensitive to the composition and conformational state of biomolecules, which has been utilized as the basis of THz spectroscopy for biomolecular detection.

Saccharides also reveal rich absorption features in THz band, as shown in Fig. 27(a). In particular, glucose and fructose have the same molecular formula $C_6H_{12}O_6$ as isomers, however, they exhibit their distinctive THz features in $0.5 \sim 4.0$ THz. And the calculated results indicate that experimental THz spectral features of glucose and fructose arise from both intramolecular and intermolecular modes, involving hydrogen

(a) Alanine, phenylalanine and tyrosine

(b) Thymine and cytosine
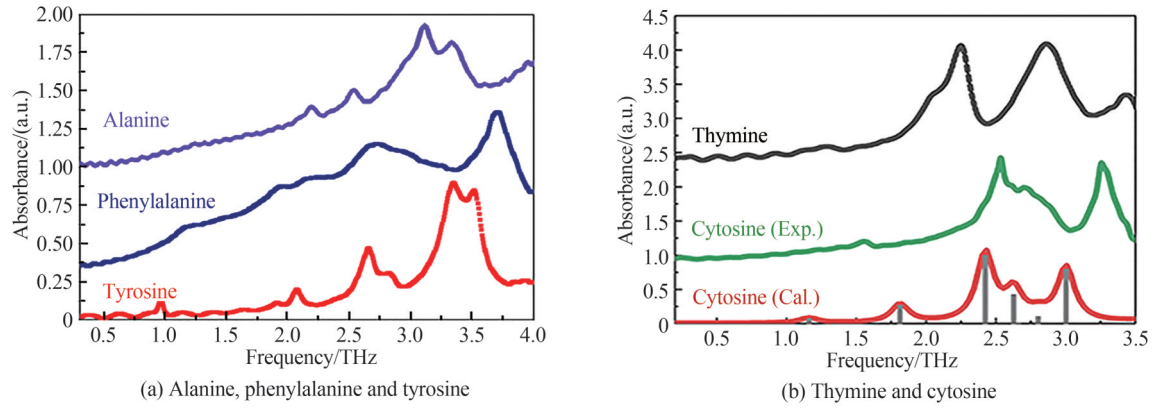
Fig. 26 THz spectra of amino acids and nucleobases

(a) Glucose, fructose, sucrose and lactose

(b) Glucose anhydrate and monohydrate
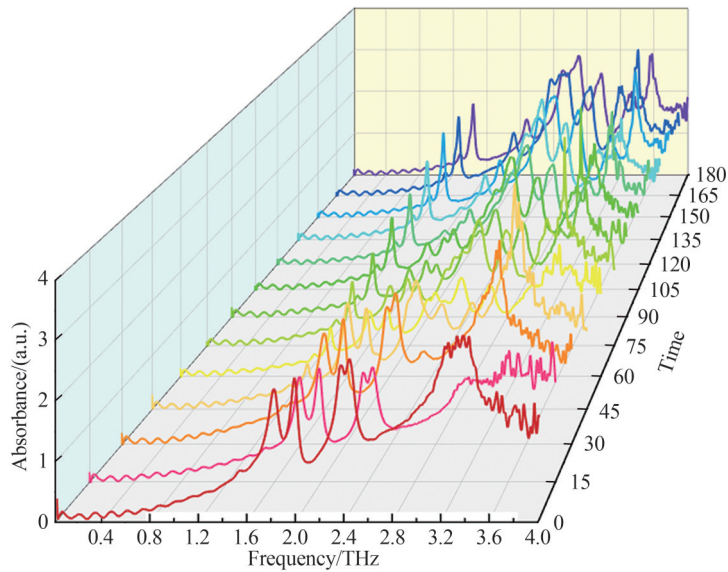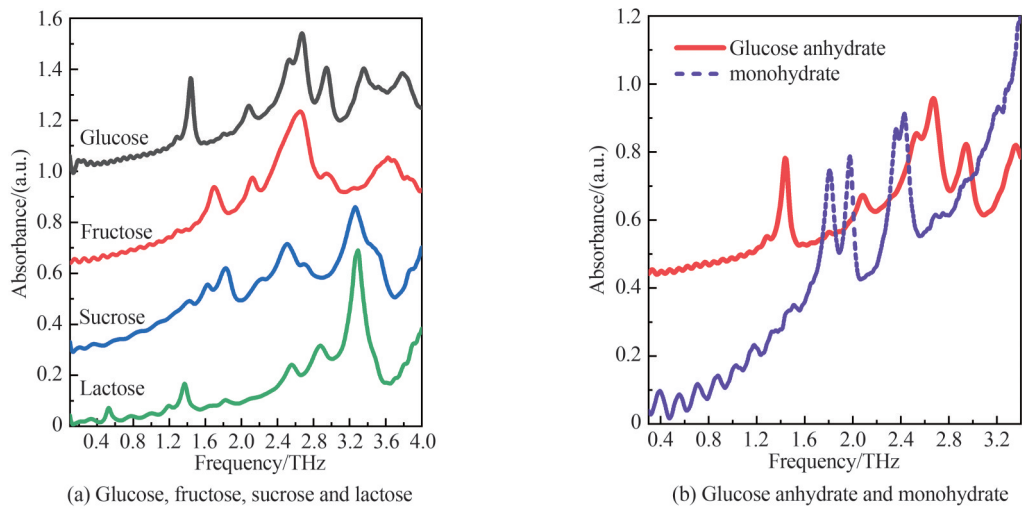
(c) THz spectral transformation of glucose monohydrate via dehydration

Fig. 27 THz spectra of saccharides

bonds and covalent bonds, and with the intermolecular modes dominating [165]. Moreover, glucose and its interesting hydrate reveal their unique THz spectral features, as shown in Fig. 27 (b). It is found that the characteristic features of monohydrated glucose ($C_6H_{12}O_6 \cdot H_2O$) mainly origin from the intermolecular modes of water-glucose and glucose-glucose molecules, while those of anhydrous glucose ($C_6H_{12}O_6$) come from

interactions of glucose molecules [166]. With dehydrating process illustrated in Fig. 27(c), the distinctive spectral features related to the hydrated structure are gradually disappeared while the spectral features at 1.44 and 2.08 THz appear in the formation of hydrogen-bond connections among glucoses, which provide clear indication for hydrogen-bond network reconstruction at the micro level [167].

6.2.2 *Organic acids and their salts*

THz spectroscopy technology has also been applied to probe intermolecular interactions of organic acids and their salts, such as sorbic acid and potassium sorbate [24], benzoic acid and sodium benzoate [168], salicylic acid and sodium salicylate [169]. The molecular structures of sorbic acid, potassium sorbate, benzoic acid and sodium benzoate are illustrated in Fig. 28(a). It can be seen clearly that the covalent bond is replaced by ionic bond after alkali Na atom replaces hydrogen atom in the hydroxyl group, resulting in the redistribution of charge density of the group. It is found that the ionic bond affects not only the bond lengths and bond angles of covalent bonds but also the arrangement composition in the cell [168, 169]. As shown in Fig. 28(b), distinct THz spectral features between organic acids and their salts are clearly observed, implying that they can be well distinguished from their characteristic spectra in THz frequency band.

(a) Molecular structures   (b) THz spectra of organic acids and their salts
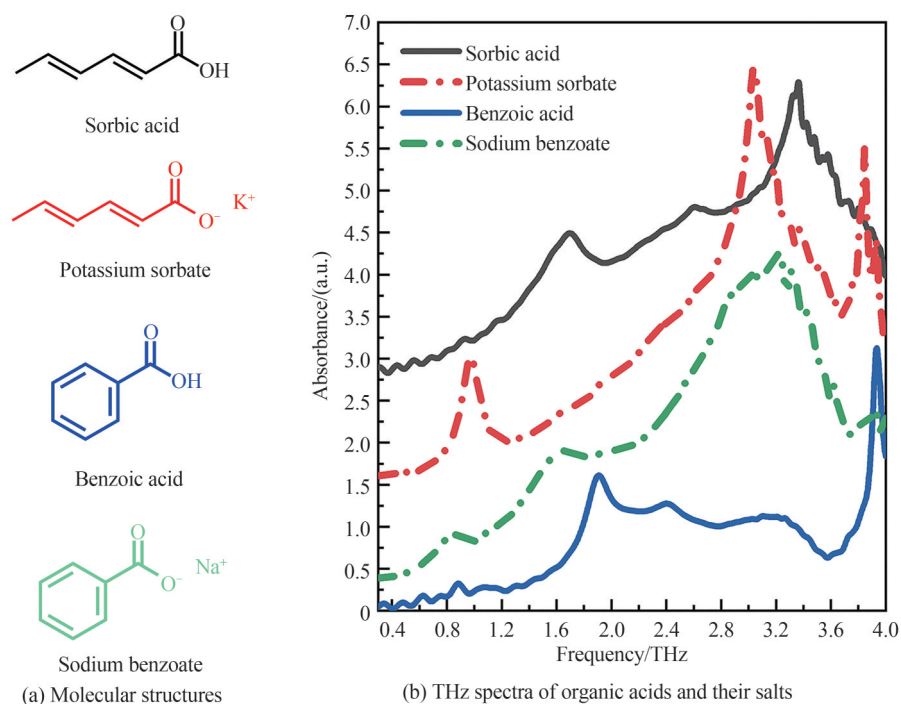
Fig. 28   Molecular structures, THz spectra of organic acids and their salts

6.2.3 *Benzenediol: constitutional isomers*

Benzene-1,2-diol (catechol), benzene-1,3-diol (resorcinol) and benzene-1,4-diol (hydroquinone), are functional group isomers in position with two hydroxyl groups attached to different positions of benzene ring. Their molecular structures are presented in Fig. 29 (a). Fig. 29 (b) shows THz absorption spectra (8~128 cm^{-1}) of these three constitutional isomers. Distinct spectral features among these THz spectra can be observed clearly, indicating that THz spectroscopy is an excellent identification tool for the constitutional isomers. Moreover, the normal modes calculated based on solid-phase density functional theory have also been utilized in assignment of experimental absorption features [170], the result shows the measured THz spectral features of benzene-1,2-diol, benzene-1,3-diol can be attributed to the intermolecular vibration. In addition, the middle infrared spectrum (400~2000 cm^{-1}) of benzene-1,2-diol is also analyzed [171]. It is found that the THz absorption peaks of benzene-1,2-diol are all derived from the intermolecular vibration, while the mid-infrared absorption peaks of benzene-1,2-diol are derived from the intramolecular vibration [171].

(a) Molecular structures

(b) THz spectra of benzenediols

(c) Benzene-1,2-diol

(d) Benzene-1,3-diol
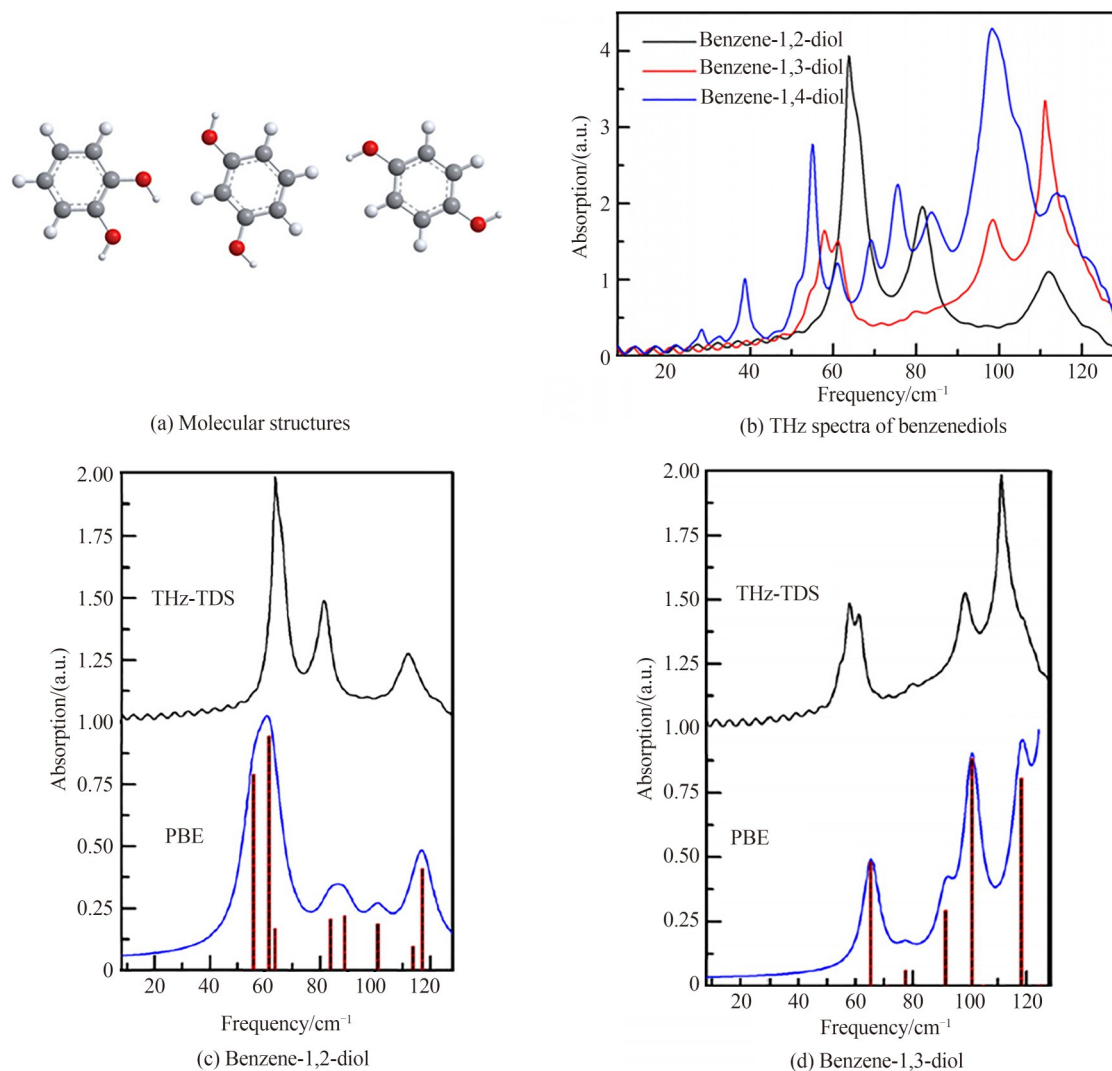
Fig. 29   THz spectra of benzenediols comparing with calculated THz spectra

6.2.4   *Chiral drug molecules: stereoisomers*

The chiral phenomenon with chiral centers in molecular structure is one of the basic elements in nature. Different enantiomers of the same chiral drug are noticeably different in pharmacological activity, the metabolic process, and toxicity because they usually achieve their pharmacological effects via strict chiral matching and molecular recognition with biological macromolecules in vivo [172, 173]. Conventional detection methods, such as High-Performance Liquid Chromatography (HPLC), polarimetry and circular dichroism, are time consuming, cumbersome operating and causing sample denaturation. Therefore, the fast, accurate, qualitative and quantitative method for the study of chiral drugs based on THz spectroscopy is proposed. Taking ibuprofen as an example, characteristic peak frequencies, peak amplitude differences and peak area differences of the enantiomers RS-ibuprofen, (R)-(-)-ibuprofen, and (S)-(+)-ibuprofen, have been extracted to qualitatively and quantitatively distinguish these three substances [174], which shows the stability and detection accuracy of THz spectroscopy are much greater than those of Raman spectroscopy in quantitative identification. Recently, SHI W N et al. designed a THz all-dielectric metasurface with crescent cylinder arrays for chiral drug sensing, chiral molecules, such as (R)-(-)-ibuprofen and (S)-(+)-ibuprofen even in 5 μL, were successfully distinguished [175]. ZHANG Z Y et al. proposed a THz polarization sensing method and a chiral metasurface to realize high-sensitive quantitative detection. Three kinds of chiral amino acids with D- and L- enantiomers in aqueous solution were also successfully distinguished, which provides new paths for the recognition of chiral molecules in a trace amount [176].

6.3 THz spectral analysis of mixtures and practical application

With the elucidation of the mechanisms determining the THz fingerprints of biomolecules, THz spectroscopy has been exploited for qualitative and quantitative analyses of various molecules. However, in actual detection scenario, most of the detection objects are multi-component mixture. Therefore, it is very urgent and practical by using THz spectroscopy to "fingerprint" and identify unknown mixed compounds.

6.3.1 *Spectral analysis of mixtures based on THz characteristic peaks*

Considering commercial glucose is probably mixture in two available forms of anhydrate and monohydrate as shown in Fig. 30(a)[177, 178], two-forms mixtures with different percentage composition have been measured by THz-TDS[167]. As shown in Fig. 30(c), THz fingerprint peaks of each glucose component could be dramatically identified from the spectra of mixtures, indicating their possible identification according to their distinct THz spectral fingerprints. Moreover, characteristic peaks at 1.44 and 1.82 THz can be specified as the main quantitative indicators for quantitative detection, which represent the content anhydrate and monohydrate, respectively.

(a) Molecular packing

(b) The linear fittings

(c) THz signatures of glucose and mixtures

(d) THz spectra of glucose powders (A, B and C)
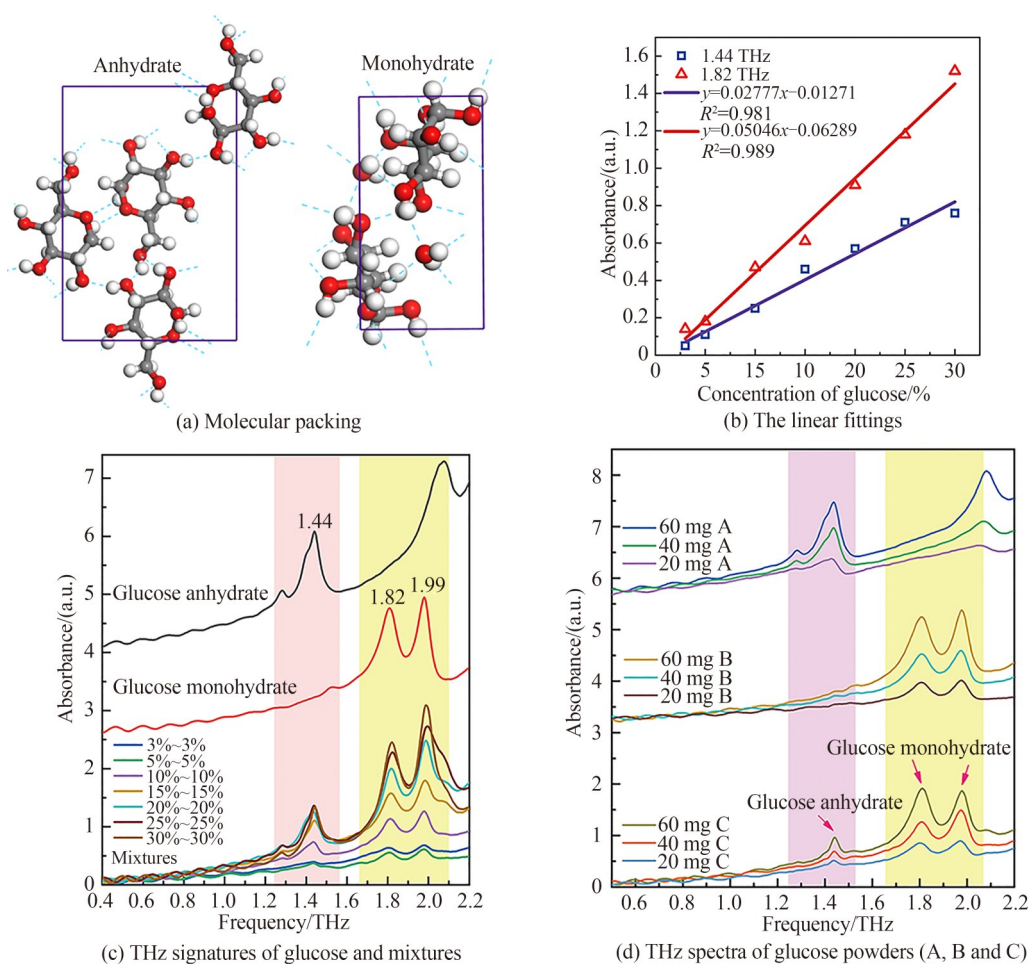
Fig. 30　THz spectral analysis of glucose anhydrate and monohydrate mixtures

As shown in Fig. 30(b), the linear relationships between peak heights and the percentage compositions are revealed, where the goodness of fit reaches to 98%. Moreover, Fig. 30(d) shows three commercially available brands of edible glucose powder A, B, C can be effectively identified by their THz spectral signatures, and also, the proportion of anhydrate and monohydrate in powder C is further quantified as 0.64:1[167]. Benefiting from the main THz fingerprint peaks of each component are coincidentally separated, it achieves a direct and effective recognition. This is a simple quantitative case in mixture's detection, which provides a new idea for the detection of anhydrated and hydrated mixture. It may be potentially shed light on industrial monitoring of glucose production and other related mixture in the future.

6.3.2 *Spectral analysis of mixtures by machine learning methods*

Because absorption features in THz frequency band are normally quite broader, consequently, the superposition of absorption features and baseline drift for complex mixtures are commonly happened, resulting in spectrum overlapping and distortion [179-181]. It is still a big challenge to achieve reliable and efficient detection of complex mixtures. Therefore, we try to analyze THz spectra of multi-component mixtures by using machine learning method [24]. In particularly, Blind Source Separation (BSS) methods [182-183] based on multivariate data analysis are competent for blind (unsupervised) extraction of components from multicomponent-mixture spectra. As shown in Fig. 31, the "unknown" multicomponent systems are measured by ultrafast THz characteristic spectroscopy based on femtosecond laser and the spectral matrix is found based on their THz spectra. Subsequently, three major challenges have been accomplished by machine learning methods. First, the number of components in mixtures is obtained by the Singular Value Decomposition (SVD) [184]. Second, the multicomponent spectra are extracted by Non-negative Matrix Factorization (NMF) [185-186] and Self-Modelling Mixture Analysis (SMMA) [187-188]. Third, the Support Vector for Regression (SVR) [189-190] designed an underlying model to the target components and simultaneously identified contents of each individual component. This approach works very well in spectral analysis of binary and ternary mixtures so far. The extracted component spectra match well with the measured THz spectra of pure reagents, and the predicted componential contents are consistent with nominal contents where the decision coefficient is up to $R^2 = 0.989$ [24]. Since the pure substance has its unique spectral characteristics in THz frequency band, by extracting component spectrum from complex system and matching with standard spectrum in THz spectra library, the retrieval efficiency of spectrum library can be greatly improved which will facilitate quick identification of multicomponent mixture and have practical significance in detection.
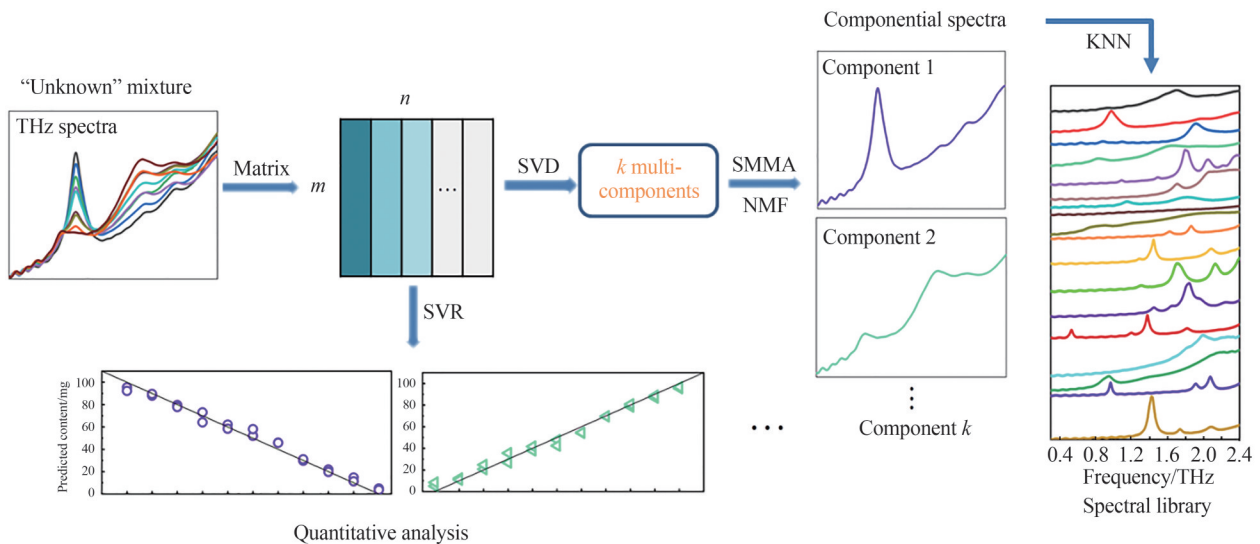
Fig. 31　Schematic diagram of analysis process for multi-component mixtures by machine learning

7　Conclusion

Impressive breakthroughs have been achieved in ultrafast THz characteristic spectroscopy based on femtosecond laser and its applications. In this review, we summarize the progress achieved in this field and discuss some challenges and strategies for implementation of practical applications. However, there still have some intrinsic limitations and technical bottlenecks of free-space THz characteristic spectroscopy that have led to some constraints about the practicability of its clinical adoption. It can only detect the sample in milligram level, and it is difficult to realize the detection of trace substance. One of the most promising routes to promote THz sensing sensitivities is to use metamaterials [146-147,191]. The excellent characteristics and practical functions of metamaterials can be mainly attributed the flexible and adjustable resonance characteristics and the local field generated by resonant excitation, which enhance the interaction between the THz wave and the detected sample, so that the current THz sources with limited power can achieve more effective and sensitive detection.

Therefore, the combination of metamaterial structure and ultrafast THz characteristic spectroscopy to enhance the sensing signal is a feasible and effective method.

References

[1] HARTER T, UMMTHHALA S, BLAICHER M, et al. Wireless THz link with optoelectronic transmitter and receiver [J]. Optica, 2019, 6: 1063-1070.

[2] TONOUCHI M. Cutting-edge terahertz technology[J]. Nature Photonics, 2007, 1(2): 97-105.

[3] XU W, XIE L, YING Y. Mechanisms and applications of terahertz metamaterial sensing: a review[J]. Nanoscale, 2017, 9 (37): 13864-13878.

[4] GRAHAM-ROWE D. Terahertz takes to the stage[J]. Nature Photonics, 2007, 1(2): 75-77.

[5] MAHIEU E, CHIPPERFIELD M P, NOTHOLT J, et al. Recent northern hemisphere stratospheric HCl increase due to atmospheric circulation changes[J]. Nature, 2014, 515: 104-107.

[6] GUERBOUKHA H, NALLAPPAN K, SKOROBOGATIY M. Exploiting k-space/frequency duality toward real-time terahertz imaging[J]. Optica, 2018, 5(2): 109-116.

[7] PAN M, CASSAR Q, FAUQUET F, et al. Guided terahertz pulse reflectometry with double photoconductive antenna [J]. Applied Optics, 2020, 59(6): 1641-1647.

[8] YARDIMCI N T, JARRAHI M. Nanostructure-enhanced photoconductive terahertz emission and detection[J]. Small, 2018, 14: 1802437.

[9] BURFORD N M, EI-SHENAWEE M O. Review of terahertz photoconductive antenna technology [J]. Optical Engineering, 2017, 56(1): 010901.

[10] AUSTON D H. Picosecond optoelectronic switching and gating in silicon[J]. Applied Physics Letters, 1975, 26(3): 101-103.

[11] GRISCHKOWSKY D, KEIDING S, VAN-EXTER M. Far-infrared time-domain spectroscopy with terahertz beams of dielectrics and semiconductors[J]. Journal of the Optical Society of America B, 1990, 7(10): 2006-2015.

[12] BAXTER J B, GUGLIETTA G W. Terahertz spectroscopy[J]. Analytical Chemistry, 2011, 83(12): 4342-4368.

[13] BANKS P A, BURGESSA L, RUGGIERO M T. The necessity of periodic boundary conditions for the accurate calculation of crystalline terahertz spectra[J]. Physical Chemistry Chemical Physics, 2021, 23(36): 20038-20051.

[14] OZAKI Y, BEĆ K B, MORISAWA Y, et al. Advances, challenges and perspectives of quantum chemical approaches in molecular spectroscopy of the condensed phase[J]. Chemical Society Reviews, 2021, 50(19):10917-10954.

[15] WALTHER M, PLOCHOCKA P, FISCHER B, et al. Collective vibrational modes in biological molecules investigated by terahertz time-domain spectroscopy [J]. Biopolymers 2002, 67: 310-313.

[16] ZHU Z J, CHENG C, CHANG C, et al. Characteristic fingerprint spectrum of neurotransmitter norepinephrine with broadband terahertz time-domain spectroscopy[J]. Analyst, 2019, 144(8): 2504-2510.

[17] PERTICAROLI S, RUSSO D, PAOLANTONI M, et al. Painting biological low-frequency vibrational modes from small peptides to proteins[J]. Physical Chemistry Chemical Physics, 2015, 17(17): 11423-11431.

[18] GONZÁLEZ-JIMÉNEZ M, RAMAKRISHNA G, HARWOOD T, et al. Observation of coherent delocalized phonon-like modes in DNA under physiological conditions[J]. Nature Communications, 2016, 7: 11799.

[19] GONZÁLEZ-JIMÉNEZ M, RAMAKRISHNAN G, TUKACHEV N V, et al. Low-frequency vibrational modes in G-quadruplexes reveal the mechanical properties of nucleic acids[J]. Physical Chemistry Chemical Physics, 2021, 23(23): 13250-13260.

[20] ESENTURK O, EVANS A, HEILWEIL E J. Terahertz spectroscopy of dicyano-benzenes: Anomalous absorption intensities and spectral calculations[J]. Chemical Physics Letters, 2007, 442(1):71-77.

[21] WALTHER M, FISCHER B, SCHALL M, et al. Far-infrared vibrational spectra of all-trans, 9-cis and 13-cis retinal measured by THz time-domain spectroscopy[J]. Chemical Physics Letters, 2000, 332(3-4): 389-395.

[22] WANG Z F, PENG Y, SHI C J, et al. Qualitative and quntitative recognition of chiral drugs based on terahertz spectroscopy[J]. Analyst, 2021, 146(12): 3888-3898.

[23] MOTLEY T L, KORTER T M. Terahertz spectroscopy and molecular modeling of 2-pyridone clusters[J]. Chemical Physics Letters, 2008, 464(4-6): 171-176.

[24] YAN H, FAN W H, CHEN X, et al. Component spectra extraction and quantitative analysis for preservative mixtures by combining Terahertz spectroscopy and machine learning[J]. Spectrochimica Acta Part A: Molecular and Biomolecular Spectroscopy, 2022, 271: 120908.

[25] YANG S H, JARRAHI M. Navigating THz spectrum via photomixing[J]. Optics and Photonics News, 2020, 31(7): 38-43.

[26] GU Z, CHEN Y, LI H, et al. Research progress of terahertz radiation sources[J]. Infrared Technology, 2011, 33(5): 252-261.

[27] DOBROIU A, YAMASHITA M, OHSHIMA Y N, et al. Terahertz imaging system based on a backward-wave

oscillator[J]. Applied Optics，2004，43(30)：5637-5646.

[28]　ESAKI L. New phenomenon in narrow Ge p-n junctions[J]. Physical Review Letters，1985，109(12)：603-606.

[29]　LI W，YAO J. Investigation of photonically assisted microwave frequency multiplication based on external modulation[J]. IEEE Transactions on Microwave Theory and Techniques，2010，58(11)：3259-3268.

[30]　RODWELL M J W，KAMEGAWA M，YU R Y，et al. GaAs nonlinear transmission lines for picosecond pulse generation and millimeter-wave sampling[J]. IEEE Transactions on Microwave Theory and Techniques，1991，39(7)：1194-1204.

[31]　MADEY J M. Stimulated emission of bremsstrahlung in a periodic magnetic field[J]. Journal of Applied Physics，1971，42(5)：1906-1913.

[32]　YEH K L，HOFFMANN M，HEBLING J，et al. Generation of 10 μJ ultrashort terahertz pulses by optical rectification[J]. Applied Physics Letters，2007，90(17)：171121.

[33]　XIE X，DAI J，ZHANG X C. Coherent control of THz wave generation in ambient air[J]. Physical Review Letters，2006，96(7)：075005.

[34]　KAWASE K，SHIKATA J I，IMAI K，et al. Transform-limited，narrow-linewidth，terahertz-wave parametric generator[J]. Applied Physics Letters，2001，78(19)：2819-2821.

[35]　SUN B，YAO J. Generation of terahertz wave based on optical methods[J]. Chinese Journal of Lasers，2006，33(10)：1349.

[36]　CURWEN C A，RENO J L，WILLIAMS B S. Terahertz quantum cascade VECSEL with watt-level output power[J]. Applied Physics Letters，2018，113(1)：4.

[37]　LIU C，ZHANG S，WANG S，et al. Active spintronic-metasurface terahertz emitters with tunable chirality[J]. Advanced Photonics，2021，3(5)：056002.

[38]　SUN R，YANG S，YANG X，et al. Large tunable spin-to-charge conversion induced by hybrid rashba and dirac surface states in topological insulator heterostructures[J]. Nano Letter，2019，19(7)：4420-4426.

[39]　HALE L L，JUNG H，GENNARO S D，et al. Terahertz pulse generation from GaAs metasurfaces[J]. ACS Photonics，2022，9(4)：1136-1142.

[40]　SAFIAN R，GHAZI，G，MOHAMMADIAN N. Review of photomixing continuous-wave terahertz systems and current application trends in terahertz domain[J]. Optical Engineering，2019，58(11)：110901.

[41]　LEWIS R A. A review of terahertz detectors[J]. Journal of Physics D：Applied Physics，2019，52：433001.

[42]　JEPSEN1 P U，COOKE D G，KOCH M. Terahertz spectroscopy and imaging-Modern techniques and applications[J]. Laser Photonics Review，2011，5(1)：124-166.

[43]　CHEN L C，FAN W H. Study on finger capacitance of terahertz photomixer in low-temperature-grown GaAs using Finite Element Method[J]. Chinese Physics B，2012，21(10)：104101.

[44]　DARROW J T，ZHANG X C，IPPEN D H. Saturation properties of large-aperture photoconducting antennas[J]. IEEE Journal of Quantum Electronics，1992，28(6)：1607-1616.

[45]　LEPESHOV S，GORODETSKY A，KRASNOK A，et al. Enhancement of terahertz photoconductive antenna operation by optical nanoantennas[J]. Laser Photonics Review，2017，11(1)：1770001.

[46]　KOHIHAAS R B，BREUER S，NELLEN，S，et al. Photoconductive terahertz detectors with 105 dB peak dynamic range made of rhodium doped InGaAs[J]. Applied Physics Letters，2019，114：221103.

[47]　CHEN L C，FAN W H. Numerical simulation of terahertz generation and detection based on ultrafast photoconductive antennas[C]. SPIE，2011，8195：81950K.

[48]　LEE Y S. Principles of Terahertz Science and Technology[M]. Springer，2009.

[49]　BERRY C W，WANG N，HASHEMI M R，et al. Significant performance enhancement in photoconductive terahertz optoelectronics by incorporating plasmonic contact electrodes[J]. Nature Communications，2013，4：1622.

[50]　STONE M R，NAFTALY M，MILES R E，et al. Electrical and radiation characteristics of semilarge photoconductive terahertz emitters[J]. IEEE Transactions on Microwave Theory and Techniques，2004，52(10)：2420-2429.

[51]　WARREN A C，KATZENELLENBOGEN N，GRISCHKOWSKY D，et al. Subpicosecond，freely propagating electromagnetic pulse generation and detection using GaAs：As epilayers[J]. Applied Physics Letters，1991，58(14)：1512-1514.

[52]　LIU T A，TANI M，NAKAJIMA M，et al. Ultrabroadband terahertz field detection by photoconductive antennas based on multi-energy arsenic-ion-implanted GaAs and semi-insulating GaAs[J]. Applied Physics Letters，2003，83(7)：1322-1324.

[53]　SUZUKI M，TONOUCHI M. Fe-implanted InGaAs terahertz emitters for 1.56 μm wavelength excitation[J]. Applied Physics Letters，2005，86(5)：1-3.

[54]　TANI M，LEE K，ZHANG X C. Detection of terahertz radiation with low-temperature-grown GaAs-based photoconductive antenna using 1.55 μm probe[J]. Applied Physics Letters，2000，77(9)：1396-1399.

［55］ SARTORIUS B，ROEHLE H，KÜNZEL H，et al. All-fiber terahertz time-domain spectrometer operating at 1.5 micron telecon wavelengths［J］. Optics Express，2008，16(13)：9565-9570.

［56］ WOOD C D，HATEM O，CUNNINGHAM J E，et al. Terahertz emission from metal-organic chemical vapor deposition grown Fe：InGaAs using 830 nm to 1.55 μm excitation［J］. Applied Physics Letters，2010，96(19)：1-4.

［57］ SIGMUND J，SYDLO C，HARTNAGEL H L，et al. Structure investigation of low-temperature-grown GaAsSb，a material for photoconductive terahertz antennas［J］. Applied Physics Letters，2005，87(25)：1-3.

［58］ GU P，TANI M，KONO S，et al. Study of terahertz radiation from InAs and InSb［J］. Journal of Applied Physics，2002，91(9)：5533-5537.

［59］ ASCÁZUBI R，SHNEIDER C，WILKE I，et al. Enhanced terahertz emission from impurity compensated GaSb［J］. Physical Review B，2005，72(4)：1-5.

［60］ ASCAZUBI R，WILKE I，KIM K J，et al. Terahertz emission from Ga$_{1-x}$In$_x$Sb［J］. Physical Review B，2006，74(7)：75323.

［61］ SALEM B，MORRIS D，AIMEZ A，et al. Improved characteristics of a terahertz set-up built with an emitter and a detetor made on proton-bombarded GaAs photoconductive materials［J］. Semiconductor Science And Technology，2006，21(3)：283-286.

［62］ LIU T A，TANI M，PAN C L. THz radiation emission properties of multienergy arsenic-ion-implanted GaAs and semi-insulating GaAs based photoconductive antennas［J］. Journal of Applied Physics，2003，93(5)：2996-3001.

［63］ TANI M，SAKAI K，ABE H，et al. Spectroscopic characterization of low-temperature grown GaAs epitaxial films［J］. Japanese Journal of Applied Physics，1994，33(9)：4807-4811.

［64］ BURYAKOVA A M，IVANOV M S，NOMOEV S A，et al. An advanced approach to control the electro-optical properties of LT-GaAs based terahertz photoconductive antenna［J］. Materials Research Bulletin，2019，122：110688.

［65］ HATEM O，CUNNINGHAM J，LINFIELD E H，et al. Terahertz-frequency photoconductive detectors fabricated from metal-organic chemical vapor deposition-grown Fe-doped InGaAs［J］. Applied Physics Letters，2011，98(12)：1-3.

［66］ FANDIO D J J，ILAHI B，DION M，et al. Ultrafast photocarrier dynamics in Fe-implanted InGaAs polycrystalline photoconductive materials［J］. Journal of Physics：Condensed Matter，2021，33：385701.

［67］ LU P K，TURAN D，MONA J，et al. High-power terahertz pulse generation from bias-free nanoantennas on graded composition InGaAs structures［J］. Optical Express，2022，2(17)：1584-1598.

［68］ DIETZ R J B，GLOBISCH B，ROEHLE H，et al. Influence and adjustment of carrier lifetimes in InGaAs/InAlAs photoconductive pulsed terahertz detectors：6 THz bandwidth and 90dB dynamic range［J］. Optics Letters，2014，22(16)：615-623.

［69］ PREU S，MITTENDORFF M，LU H，et al. 1550 nm ErAs：In(Al)GaAs large area photoconductive emitters［J］. Applied Physics Letters，2012，101(10)：1-3.

［70］ KIM D S，CITRIND S. Coulomb and radiation screening in photoconductive terahertz sources［J］. Applied Physics Letters，2006，88(16)：86-89.

［71］ BUDIARTO E，MARGOLIES J，JEONG S，et al. High-intensity terahertz pulses at 1-kHz repetition rate［J］. IEEE Journal of Quantum Electronics，1996，32(10)：1839-1846.

［72］ YAN Z，SHI W. Radiation characteristics of terahertz GaAs photoconductive antenna arrays［J］. Acta Physica Sinica，2021，70：248704.

［73］ BERRY C W，HASHEMI M R，JARRAHI M. Generation of high power pulsed terahertz radiation using a plasmonic photoconductive emitter array with logarithmic spiral antennas［J］. Applied Physics Letters，2014，104(8)：081122.

［74］ SHI W，WANG Z，LI C，et al. New antenna for detecting polarization states of terahertz［J］. Frontiers in Physics，2022，10：850770.

［75］ DREYHAUPT A，WINNERL S，DEKORSY T，et al. High-intensity terahertz radiation from a microstructured large-area photoconductor［J］. Applied Physics Letters，2005，86(12)：1-3.

［76］ ACUNA G，BUERSGENS F，LANG C，et al. Interdigitated terahertz emitters［J］. Electronics Letters，2008，44(3)：229-231.

［77］ ROPAGNOL X，LSGANDAROV E，CHAI X，et al. Generation of intense sub-cycle terahertz pulses with variable elliptical polarization［J］. Applied Physics Letters，2022，120：171106.

［78］ LIU W，ZHANG Z，SU Q，et al. Interdigitated photoconductive antenna-based two-color femtosecond laser filamentation THz time-domain spectral detection［J］. Optics Express，2022，30(11)：18562-18570.

［79］ BOBY E N F，PRAJAPATI J，RATHINASAMY V，et al. Parametric investigation of interdigitated photoconductive antenna for efficient terahertz applications［J］. Arabian Journal for Science and Engineering，2022，47(3)：3597-3609.

［80］ UPADHYA P C，FAN W H，BURNETT A，et al. Excitation-density-dependent generation of broadband terahertz radiation in an asymmetrically excited photoconductive antenna［J］. Optics Letters，2007，32(16)：2297-2299.

［81］ DIONNE J A，SWEATLOCK L A，ATWATER H A，et al. Planar metal plasmon waveguides：frequency-dependent

dispersion, propagation, localization, and loss beyond the free electron model[J]. Physical Review B, 2005, 72: 075405.

[82] PARK S G, JIN K H, YI M, et al. Enhancement of terahertz pulse emission by optical nanoantenna[J]. ACS Nano, 2012, 6(3): 2026-2031.

[83] JOOSHESH A, BAHRAMI-YEKTA V, ZHANG J, et al. Plasmon-enhanced below bandgap photoconductive terahertz generation and detection[J]. Nano Letters, 2015, 15: 8306.

[84] BASHIRPOUR M, POURSAFAR J, KOLAHDOUZ M, et al. Terahertz radiation enhancement in dipole photoconductive antenna on LT-GaAs using a gold plasmonic nanodisk array[J]. Optics and Laser Technology, 2019, 120: 105726.

[85] YANG S H, HASHEMI M R, BERRY C W, et al. 7.5% optical-to-terahertz conversion efficiency offered by photoconductive emitters with three-dimensional plasmonic contact electrodes[J]. IEEE Transaction on Terahertz Science and Technology, 2014, 4(5): 575-581.

[86] HESHMAT B, PAHLEVANINEZHAD H, PANG Y, et al. Nanoplasmonic terahertz photoconductive switch on GaAs [J]. Nano Letters, 2012, 12: 6255.

[87] BERRY C W, HASHEMI M R, PREU S, et al. High power terahertz generation using 1550 nm plasmonic photomixers [J]. Applied Physics Letters, 2014, 105: 011121.

[88] WANG N, CAKMAKYAPAN S, LIN Y J, et al. Room-temperature heterodyne terahertz detection with quantum-level sensitivity[J]. Nature Astronomy, 2019, 3(11): 977-982.

[89] BARDOLAZA H R, CABELLO N I F, FERROLINO J P R, et al. Integrated optics spiral photoconductive antennas coupled with 1D and 2D micron-size terahertz-wavelength plasmonic metal arrays[J]. Optical Materials Express, 2022, 12 (4): 1617-1626.

[90] YARDIMCI N T, YANG S H, BERRY C W, et al. High-power terahertz generation using large-area plasmonic photoconductive emitters[J]. IEEE Transactions on Terahertz Science and Technology, 2015, 5(2): 223-229.

[91] YARDIMCI N T, LU H, JARRAHI M, et al. High power telecommunication-compatible photoconductive terahertz emitters based on plasmonic nano-antenna arrays[J]. Applied Physics Letters, 2016, 109(19): 284-286

[92] YARDIMCI N T, JARRAHI M. High sensitivity terahertz detection through large-area plasmonic nano-antenna arrays [J]. Scientific Reports, 2017, 7: 42667.

[93] TURAN D, YARDIMCI N T, JARRAHI M. Plasmonics-enhanced photoconductive terahertz detector pumped by Ytterbium-doped fiber laser[J]. Optics Express, 2020, 28(3): 3835-3845.

[94] MITROFANOV O, BRENER I, LUK T S, et al. Photoconductive terahertz near-field detector with a hybrid nanoantenna array cavity[J]. ACS Photonics, 2015, 2(12): 1763-1768.

[95] YARDIMCI N T, CAKMAKYAPAN S, HEMMATI S, et al. A high-power broadband terahertz source enabled by three-dimensional light confinement in a plasmonic nanocavity[J]. Scientific Reports, 2017, 7: 4166.

[96] BURFORD N M, EVANS M J, EL-SHENAWEE M O. Plasmonic nanodisk thin-film terahertz photoconductive antenna[J]. IEEE Transactions on Terahertz Science and Technology, 2017, 8: 237-247.

[97] JIANG X Q, FAN W H, SONG C, et al. Terahertz photoconductive antenna based on antireflection dielectric metasurfaces with embedded plasmonic nanodisks[J]. Applied Optics, 2021, 60(26): 7921-7928.

[98] KHORSHIDI M, DADASHZADEH G. Dielectric structure with periodic strips for increasing radiation power of photoconductive antennas: theoretical analysis[J]. Journal of Infrared, Millimeter, and Terahertz Waves, 2017, 38(5): 609-629.

[99] MITROFANOV O, SIDAY T, THOMPSON R J, et al. Efficient photoconductive terahertz detector with all-dielectric optical metasurface[J]. APL Photonics, 2018, 3(5): 051703.

[100] CABELLO N I, REYES A D L, SARMIENTO V, et al. Terahertz emission enhancement of gallium-arsenide-based photoconductive antennas by silicon nanowire coating[J]. IEEE Transactions on Terahertz Science and Technology, 2022, 12(1): 36-41.

[101] WANG K M, GU J Q, SHI W Q, et al. All-dielectric nanograting for increasing terahertz radiation power of photoconductive antennas[J]. Optics Express, 2020, 28(13): 19144-19151.

[102] SIDAY T, VABISHCHEVICH P P, HALE L, et al. Terahertz detection with perfectly-absorbing photoconductive metasurface[J]. Nano Letters, 2019, 19(5): 2888-2896.

[103] HALE L L, HARRIS C T, LUK T S, et al. Highly efficient terahertz photoconductive metasurface detectors operating at microwatt-level gate powers[J]. Optics Letters, 2021, 46(13): 3159-3162.

[104] KUZNETSOV K A, SAFRONENKOV D A, KUZNETSOV PETR I, et al. Terahertz photoconductive antenna based on a topological insulator nanofilm[J]. Applied Sciences, 2021, 11: 5580.

[105] OKAMOTO T, FUJIMURA N, CRESPI L, et al. Terahertz detection with an antenna-coupled highly-doped silicon quantum dot[J]. Scientific Reports, 2019, 9: 18574.

[106] LI H, FAN W H, LIU J. Analysis of terahertz generation characteristic affected by injured photoconductive antenna[C].

SPIE, 2013: 8909: 89090I.

[107] LI H, FAN W H, Liu J. Investigation on terahertz generation by controlling the laser spot size on photoconductive antenna[J]. Infrared and Laser Engineering, 2015, 44(3): 528-533.

[108] SHEN T C, GAO G B, MORKOC H. Recent developments in ohmic contacts for III-V compound semiconductors[J]. Journal of Vacuum Science and Technology B, 1992, 10(5): 2113-2132.

[109] PIOTROWSKA A, GUIVARC H A, PELOUS G. Ohmic contacts to III-V compound semiconductors: A review of fabrication techniques[J]. Solid State Electronics, 1983, 26(3): 179-197.

[110] MURAKAMI M. Development of ohmic contact materials for GaAs integrated circuits[J]. Materials Science Reports, 1990, 5(5): 273-317.

[111] TURAN D, CORZO-GARCIA S C, YARDIMCI N T, et al. Impact of the metal adhesion layer on the radiation power of plasmonic photoconductive terahertz sources[J]. Journal of Infrared, Millimeter, and Terahertz Waves, 2017, 38: 1448-1456.

[112] LILIENTAL-WEBER Z, NEWMAN N, WASHBURN J, et al. Influence of interfacial contamination on the structure and barrier height of Cr/GaAs Schottky contacts[J]. Applied Physics Letters, 1989, 54(4): 356-358.

[113] SPICER W E, NEWMAN N, SPINDT C J, et al. "Pinning" and Fermi level movement at GaAs surfaces and interfaces [J]. Journal of Vacuum Science and Technology A, 1998, 8(8): 2084-2089.

[114] LEITENSTORFER A, HUNSCHE S, SHAH J, et al. Detectors and sources for ultrabroadband electro-optic sampling: Experiment and theory[J]. Applied Physics Letters, 1999, 74(11): 1516-1518.

[115] LEAHY-HOPPA M R, FITCH M J, OSIANDER R. Terahertz spectroscopy techniques for explosives detection[J]. Analytical and Bioanalytical Chemistry, 2009, 395(2): 247-257.

[116] JEPSEN P U, FISCHER B M. Dynamic range in terahertz time-domain transmission and reflection spectroscopy[J]. Optics Letters, 2005, 30(1): 29-31.

[117] MCINTOSH A I, YANG B, GOLDUP S M, et al. Terahertz spectroscopy: a powerful new tool for the chemical sciences?[J]. Chemical Society Reviews, 2012, 41: 2072-2082.

[118] DAVIES A G, BURNETT A D, FAN W H, et al. Terahertz spectroscopy of explosives and drugs[J]. Materials Today, 2008, 11(3): 18-26.

[119] UENO Y, RUNGSAWANG R, TOMITA I, et al. Quantitative measurements of amino acids by terahertz time-domain transmission spectroscopy[J]. Analytical Chemistry, 2006, 78: 5424-5428.

[120] ZHU Z J, ZHANG J B, SONG Y S, et al. Broadband terahertz signatures and vibrations of dopamine[J]. Analyst, 2020, 145: 6006-6013.

[121] YANG X, ZHAO X, YANG K, et al. Biomedical applications of terahertz spectroscopy and imaging[J]. Trends in Biotechnology, 2016, 34(10): 810-824.

[122] SUN Q S, HE Y Z, LIU K, et al. Recent advances in terahertz technology for biomedical applications[J]. Quantitative Imaging in Medicine and Surgery, 2017, 7(3): 345-355.

[123] SIBIK J, ZEITLER J A. Direct measurement of molecular mobility and crystallization of amorphous pharmaceuticals using terahertz spectroscopy[J]. Advanced Drug Delivery Reviews, 2016, 100(1): 147-157.

[124] PATIL M R, GANORKAR S. B, PATIL A S, et al. Terahertz spectroscopy: Encoding the discovery, instrumentation, and applications toward pharmaceutical prospective [J]. Critical Reviews in Analytical Chemistry, 2022, 52(2): 343-355.

[125] NGUYEN K L, FRISCIĆ T, DAY G M, et al. Terahertz time-domain spectroscopy and the quantitative monitoring of mechanochemical cocrystal formation[J]. Nature Materials, 2007, 6(3): 206-209.

[126] MITRYUKOVSKIY S, VANPOUCKE D E P, BAI Y, et al. On the influence of water on THz vibrational spectral features of molecular crystals[J]. Physical Chemistry Chemical Physics, 2022, 24(10): 6107-6125.

[127] MOTTI S G, PATEL J B, OLIVER R D J, et al. Phase segregation in mixed-halide perovskites affects charge-carrier dynamics while preserving mobility[J]. Nature Communication, 2021, 12(1): 6955.

[128] TAYVAH U T, NEU J, SPIES J A, et al. Ultrafast terahertz spectroscopy provides insight into charge transfer efficiency and dynamics in artificial photosynthesis[J]. Photosynthesis Research, 2022, 151(2): 145-153.

[129] BOSELEY R E, VONGSVIVUT J, APPADOO D, et al. Monitoring the chemical changes in fingermark residue over time using synchrotron infrared spectroscopy[J]. Analyst, 2022, 147(5): 799-810.

[130] CONSOLINO L, BARTALINI S, NATALE D P. Terahertz frequency metrology for spectroscopic applications: a review[J]. Journal of Infrared Millimeter and Terahertz Waves, 2017, 38(11): 1289-1315.

[131] WILMINK G J, IBEY B L, TONGUE T, et al. Development of a compact terahertz time-domain spectrometer for the measurement of the optical properties of biological tissues[J]. Journal of Biomedical Optics, 2011, 16(4): 047006.

[132] PAL S K, PEON J, ZEWAIL A H. Biological water at the protein surface: dynamical solvation probed directly with femtosecond resolution[J]. Proceedings of the National Academy of Sciences, 2002, 99(4): 1763-1768.

[133] BORN B, KIM S J, EBBINGHAUS S, et al. The terahertz dance of water with the proteins：the effect of protein flexibility on the dynamical hydration shell of ubiquitin[J]. Faraday Discussion, 2009, 141：161-173.

[134] AMARLOO H, SAFAVI-NAEINI S. Enhanced on-chip terahertz vibrational absorption spectroscopy using evanescent fields in silicon waveguide structures[J]. Optics Express, 2021, 29(11)：17343.

[135] SHIRAGA K, YUICHI O, NAOSHI K, et al. Evaluation of the hydration state of saccharides using terahertz time-domain attenuated total reflection spectroscopy[J]. Food Chemistry, 2013, 140：315-320.

[136] MICKAN S P, MENIKH A, LIU H, et al. Label-free bioaffinity detection using terahertz technology[J]. Physics in Medicine and Biology, 2002, 47：3789-3795.

[137] ALFIHED S, HOLZMAN J F, FOULDSA I G. Developments in the integration and application of terahertz spectroscopy with microfluidics[J]. Biosensors and Bioelectronics, 2020, 165：112393.

[138] SHEN S L, LIU X D, SHEN Y C, et al. Recent advances in the development of materials for terahertz metamaterial sensing[J]. Advanced Optical Materials, 2022, 10：2101008.

[139] JAHANI S, JACOB Z. All-dielectric metamaterials[J]. Nature Nanotechnology, 2016, 11：23-36.

[140] CHEN X, FAN W H, SONG C. Multiple plasmonic resonance excitations on graphene metamaterials for ultrasensitive terahertz sensing[J]. Carbon, 2018, 133：416-422.

[141] LI H, XU W H, CUI Q, et al. Theoretical design of a reconfigurable broadband integrated metamaterial terahertz device [J]. Optics Express, 2020, 28(26)：40060-40074.

[142] WALIA S, SHAH C M, GUTRUF P, et al. Flexible metasurfaces and metamaterials：A review of materials and fabrication processes at micro- and nano-scales[J]. Applied Physics Reviews, 2015, 2：11303.

[143] SILALAHI H M, SHIH Y H, LIN S H, et al. Electrically controllable terahertz metamaterials with large tunabilities and low operating electric fields using electrowetting-on-dielectric cells[J]. Optics Letters, 2021, 46(23)：5962-5965.

[144] CHEN X, FAN W H. Toroidal metasurfaces integrated with microfluidic for terahertz refractive index sensing [J]. Journal of Physics D：Applied Physics, 2019, 52：485104.

[145] PENDRY J B, MARTÍN-MORENO L, GARCIA-VIDAL F J. Mimicking surface plasmons with structured surfaces [J]. Science, 2004, 305：847-848.

[146] JIANG X Q, FAN W H, CHEN X, et al. Ultrahigh-Q terahertz sensor based on simple all-dielectric metasurface with toroidal dipole resonance[J]. Applied Physics Express, 2021, 14：102008.

[147] CHEN X, FAN W H, JIANG X Q, et al. High-Q toroidal dipole metasurfaces driven by bound states in the continuum for ultrasensitive terahertz sensing[J]. Journal of Lightwave Technology, 2022, 40(7)：2181-2190.

[148] GUPTA M, SRIVASTAVA Y K, MANJAPPA M, et al. Sensing with toroidal metamaterial[J]. Applied Physics Letters, 2017, 110：121108.

[149] TANG C, CHEN J, WANG Q, et al. Toroidal dipolar response in metamaterials composed of metal-dielectric-metal sandwich magnetic resonators[J]. IEEE Photonics Journal, 2016, 8(3)：1-9.

[150] WANGY Y, HANZ Z, DUY Y, et al. Ultrasensitive terahertz sensing with high-Q toroidal dipole resonance governed by bound states in the continuum in all-dielectric metasurface[J]. Nanophotonics, 2021, 1：1295-1307.

[151] ZENG T Y, LIU G D, WANG L L, et al. Light-matter interactions enhanced by quasi-bound states in the continuum in a graphene-dielectric metasurface[J]. Optics Express, 2021, 29(24)：40177-40186.

[152] XU J J, LIAO D G, GUPTA M, et al. Terahertz microfluidic sensing with dual-torus toroidal metasurfaces [J]. Advanced Optical Materials, 2021, 9：2100024.

[153] AHMADIVAND A, GERISLIOGLU B, TOMITAKA A, et al. Extreme sensitive metasensor for targeted biomarkers identification using colloidal nanoparticles-integrated plasmonic unit cells[J]. Biomedical Optics Express, 2018, 9(2)：373-386.

[154] HAN B J, HAN Z H, QIN J Y, et al. A sensitive and selective terahertz sensor for the fingerprint detection of lactose [J]. Talanta, 2019, 192：1-5.

[155] HARTREE D R. The wave mechanics of an atom with a non-coulomb central field. I. Theory and methods[J]. Proceedings of the Cambridge Philosophical Society, 1928, 24：89-110.

[156] MOLLER C, PLESSET M S. Note on the approximation treatment for many-electron systems[J]. Physical Review, 1934, 46：618-622.

[157] HOHENBERG P, KOHN W. Inhomogeneous electron gas[J]. Physical Review, 1964, 136：B864-B871.

[158] STEPHENS P J, DEVLIN F J, CHABALOWSKI C F, et al. *Ab initio* calculation of vibrational absorption and circular dichroism spectra using density functional force fields[J]. Journal of Physical Chemistry, 1994, 98：11623-11627.

[159] BECKE A D. Density-functional thermochemistry. III. The role of exact exchange[J]. Journal of Chemical Physics, 1993, 98：5648-5652.

[160] PERDEW J P, BURKE K, ERNZERHOF M. Generalized gradient approximation made simple[J]. Physics Review Letters, 1996, 77(18)：3865-3868.

［161］ PERDEW J P, CHEVARY J A, VOSKO S H, et al. Atoms, molecules, solids, and surfaces: applications of the generalized gradient approximation for exchange and correlation［J］. Physical Review B, 1992, 46: 6671-6687.

［162］ ANDREWS S B, BURTON N A, HILLIER I H, et al. Molecular electronic structure calculations employing a plane wave basis: a comparison with Gaussian basis calculations［J］. Chemical Physics Letters, 1996, 261: 521-526.

［163］ YAN H, FAN W H, ZHENG Z P. Terahertz spectroscopy and theoretical analysis of DNA nucleobases: cytosine and thymine［J］. Spectroscopy and Spectral Analysis, 2013, 33: 2612-2616.

［164］ ZHENG Z P, FAN W H, First principle investigation of L-alanine in terahertz region［J］. Journal of Biological Physics, 2012, 38: 405-413.

［165］ ZHENG Z P, FAN W H, LIANG Y Q, et al. Application of terahertz spectroscopy and molecular modeling in isomers investigation: Glucose and fructose［J］. Optics Communication, 2012, 285: 1868-1871.

［166］ ZHENG Z P, FAN W H, LI H, et al. Terahertz spectral investigation of anhydrous and monohydrated glucose using terahertz spectroscopy and solid-state theory［J］. Journal of Molecular Spectroscopy, 2014, 296: 9-13.

［167］ YAN H, FAN W H, CHEN X, et al. Terahertz signatures and quantitative analysis of glucose anhydrate and monohydrate mixture［J］. Spectrochimica Acta Part A: Molecular and Biomolecular Spectroscopy, 2021, 258: 119825.

［168］ ZHENG Z P, FAN W H, YAN H. Study on THz spectra and vibrational modes of benzoic acid and sodium benzoate［J］. Spectroscopy and Spectral Analysis, 2013, 33: 582-585.

［169］ DING L, FAN W H, SONG C, et al. Terahertz spectroscopic investigation of salicylic acid and sodium salicylate［J］. Journal of Applied Spectroscopy, 2019, 85: 1143-1150.

［170］ ZHENG Z P, FAN W H, YAN H. Terahertz absorption spectra of benzene-1,2-diol, benzene-1,3-diol and benzene-1, 4-diol［J］. Chemical Physics Letters, 2012, 525-526: 140-143.

［171］ ZHENG Z P, FAN W H, YAN H, et al. Terahertz and mid-infrared spectroscopy of benzene-1,2-diol［J］. Journal of Molecular Spectroscopy, 2012, 281: 13-17.

［172］ WNENDT S, ZWINGENBERGER K. Thalidomide's chirality［J］. Nature, 1997, 385: 303-304.

［173］ TAO W A, GOZZO F C, COOKS R G. Mass spectrometric quantitation of chiral drugs by the kinetic method［J］. Analytical Chemistry, 2001, 73: 1692-1698.

［174］ WANG Z F, PENG Y, SHI C J, et al. Qualitative and quantitative recognition of chiral drugs based on terahertz spectroscopy［J］. Analyst, 2021, 146: 3888-3898.

［175］ SHI W N, FAN F, ZHANG Z Y, et al. Terahertz sensing for R/S chiral ibuprofen via all-dielectric metasurface with higher-order resonance［J］. Applied Sciences, 2021, 11: 8892.

［176］ ZHANG Z Y, ZHONG C Z, FAN F, et al. Terahertz polarization and chirality sensing for amino acid solution based on chiral metasurface sensor［J］. Sensors and Actuators: B. Chemical, 2021, 330: 129315.

［177］ BROWN G M, LEVY H A. α-D-Glucose: further refinement based on neutron-diffraction data［J］. Acta Crystallographica Section B, 1979, 35: 656-659.

［178］ HOUGH E, NEIDLE S, ROGERS D, et al. The crystal structure of α-D-glucose monohydrate［J］. Acta Crystallographica Section B, 1973, 29: 365-367.

［179］ HADDAD J E, MIOLLIS F D, SLEIMAN J B, et al. Chemometrics applied to quantitative analysis of ternary mixtures by terahertz spectroscopy［J］. Analytical Chemistry, 2014, 86(10): 4927-4933.

［180］ PENG Y, YUAN X R, ZOU X, et al. Terahertz identification and quantification of neurotransmitter and neurotrophy mixture［J］. Biomedical Optics Express, 2016, 7(11): 4472-4479.

［181］ JING Q F, LIU D M, TONG J C. Study on the scattering effect of terahertz waves in near-surface atmosphere［J］. IEEE Access, 2018, 6: 49007-49018.

［182］ BELOUCHRANI A, ABEDMERAIM K, CARDOSO J F, et al. A blind source separation technique using second-order statistics［J］. IEEE Transactions on Signal Processing, 1997, 45(2): 434-444.

［183］ ZHEN L L, PENG D Z, YI Z, et al. Underdetermined blind source separation using sparse coding［J］. IEEE Transactions on Neural Networks and Learning Systems, 2017, 28(12): 3102-3108.

［184］ PANMAN M R, BODIS P, SHAW D J, et al. Time-resolved vibrational spectroscopy of a molecular shuttle［J］. Physical Chemistry Chemical Physics, 2012, 6: 1865-1875.

［185］ LEE D D, SEUNG H S. Learning the parts of objects by non-negative matrix factorization［J］. Nature, 1999, 401: 788-791.

［186］ PAN J J, GILLIS N. Generalized separable nonnegative matrix factorization［J］. IEEE Transactions on Pattern Analysis and Machine Intelligence, 2021, 43(5): 1546-1561.

［187］ WINDIG W, MARKEL S. Simple-to-use interactive self-modeling mixture analysis of FTIR microscopy data［J］. Journal of Molecular Structure, 1993, 292: 161-170.

［188］ WINDIG W, ANTALEK B, LIPPERT J L, et al. Combined use of conventional and second-derivative data in the SIMPLISMA self-modeling mixture analysis approach［J］. Analytical Chemistry, 2002, 74(6): 1371-1379.

［189］ SMOLA A J, SCHOLKOPF B. A tutorial on support vector regression［J］. Statistics and Computing, 2004, 14（3）: 199-222.

［190］ ZHENG W W, TIAN D J, WANG X, et al. Support vector machine: classifying and predicting mutagenicity of complex mixtures based on pollution profiles［J］. Toxicology, 2013, 313: 151-159.

［191］ AHMADIVAND A, GERISLIOGLU B, RAMEZANI Z. Functionalized terahertz plasmonic metasensors: Femtomolar-level detection of SARS-CoV-2 spike proteins［J］. Biosensors and Bioelectronics, 2021, 177: 112971.

Ultrafast Terahertz Characteristic Spectroscopy Based on Femtosecond Laser and Its Application（Invited）

FAN Wenhui, YAN Hui, JIANG Xiaoqiang, CHEN Longchao, ZHENG Zhuanping, LIU Jia, LI Hui, DING Ling, SONG Chao

（*State Key Laboratory of Transient Optics and Photonics, Xi'an Institute of Optics and Precision Mechanics, Chinese Academy of Sciences, Xi'an 710119, China*）

Abstract: Terahertz (THz) waves (0.1 THz $\sim$ 10 THz, 1 THz $= 10^{12}$ Hz) locate in the transitional region of the electromagnetic spectrum, between the classical electronics (radio, microwave and millimeter wave) and the photonics (infrared, visible, ultraviolet and x-ray). As a kind of coherent measurement technology in THz frequency range, THz characteristic spectroscopy, with high sensitivity, rapidness and nondestructive testing as well as other unique advantages, has shown an attractive promising application prospect in detection, analysis and identification of biochemical molecules and materials. As the widely used broadband THz wave source, THz Photoconductive Antenna (THz-PCA) can emit broadband THz radiation. Therefore, as one of the promising THz emitters and detectors, THz-PCA has the advantages to overcome the defects confronted by other devices (e. g., low operation frequency, strict working condition and bulk size) and these unique advantages have made THz-PCA become the most commonly utilized THz sources in THz Time-Domain Spectroscopy (THz-TDS). Although a variety of THz-PCAs are commercially available and become indispensable in many practical applications currently, the insufficient radiation THz power still hinder the further development of THz technologies based on THz-PCA. In order to further promote the research interests of THz-PCA, the working mechanism and some new research progress, technical challenges in the process of practical application and strategies of THz-PCA have to be discussed and analyzed. The underlying physical mechanism of the transient response in THz-PCA emitter and detector are investigated, as well as the influence of several parameters including the power intensity of femtosecond pump laser, the laser pulse duration and the carrier lifetime of the substrate material, are also analyzed based on theoretical models, which provide the technical foundation for designing the efficient THz-PCA. Moreover, a plenty of valuable research schemes have been proposed to develop the THz technologies based on THz-PCA in the past decades, including photoconductive materials and structure design of THz-PCA. To be specific, the sub-picosecond carrier life time of photoconductor can be realized by creating a massive density of defects, dislocations and scattering centers in the substrate material. As for structure design of THz-PCA, the previous researches on THz-PCA was mainly focused on the saturation effect at high pump power and the large aperture dipoles, dipole arrays and interdigitated electrodes structures have been investigated during the early stage. In the recent years, as the quick development of micro-nano fabrication technologies, the THz-PCA incorporated with plasmonic nanostructures and all-dielectric nanostructures have also been widely investigated for improving its performances.

In this paper, the working principle and development status of THz-PCAs based on ultrashort pulsed laser are introduced, including theoretical models, substrate materials and different structures of photoconductive antennas. Furthermore, with the dramatic development of source and detector components, THz spectroscopy technology has been utilized in various fields such as chemical detection and substance identification, biomedical application and pharmaceutical industry. THz-TDS is the most commonly used technique in current commercial THz spectroscopy, which has attracted wide attention for

its spectral fingerprint, high temporal-spatial resolution, noninvasive and nonionizing properties. Various important biomolecules, such as amino acids, nucleobases and saccharides reveal rich absorption features in THz range. It is verified that THz spectral features originate from the collective molecules of low frequency vibration, rotation and weak interaction with the surrounding molecules (hydrogen bonding, van der Waals force, etc.), so they are very sensitive to the molecular structure and surrounding environment. It is a powerful tool to investigate molecular conformation, positional isomerism of functional groups, intermolecular interactions of organic acids and their salts, optical isomerism, etc. However, it is worth noting that the investigated targets are usually in the form of multi-component mixtures in actual scenario. When the spectral features became more complicated, the much broader THz features would be severely overlapped and accompanied by baseline drift in THz spectra. Identification and quantitative analysis of complex multi-component mixtures will become a great challenge for THz spectral analysis. To overcome such problem, a practical strategy has been proposed by combining machine learning methods with THz-TDS for implementation of practical applications. Moreover, another issue worth noting is conventional free-standing spectroscopy measurement devices are hardly adequate for the detection of microgram level or trace substance. Combination of metamaterials and conventional free-standing THz spectroscopy to enhance the sensing signal is a feasible and effective method, which is crucial for the practicability of clinical adoption. Furthermore, some recent progress we have achieved in THz characteristic spectral technology and its applications are also summarized and discussed.

Key words: Terahertz waves; Photoconductive antenna; Femtosecond laser; Characteristic spectroscopy; Substance identification; Machine learning

OCIS Codes: 300.6495; 320.7130; 140.7090; 300.6495; 120.7280